A correction to the Hamiltonian of the QCD string with quarks due to the rigidity term

D. V. Antonov

Institute of Theoretical and Experimental Physics 117218 Moscow, Russia; Institut für Elementarteilchenphysik, Humboldt-Universität, D-10115 Berlin, Germany

(Submitted 26 March, 1997)
Pis'ma Zh. Éksp. Teor. Fiz. **65**, No. 9, 673–678 (10 May 1997)

The correction to the Hamiltonian of a quark–antiquark system due to the rigidity term in the action of the gluodynamics string is found using the action obtained by D. V. Antonov *et al.*, Mod. Phys. Lett. A **11**, 1905 (1996) with the Hamiltonian obtained by A. Yu. Dubin *et al.*, Phys. At. Nucl. **56**, 1745 (1993); Phys. Lett. B **323**, 41 (1994) and E. L. Gubankova and A. Yu. Dubin, Phys. Lett. B **334**, 180 (1994); preprint ITEP 62-94. This correction contains additional contributions to the orbital momentum of the system and several higher derivative operators. The resulting Hamiltonian is used to evaluate the rigid-string-induced term in the Hamiltonian of the relativistic quark model for the case of large masses of the quark and antiquark. © *1997 American Institute of Physics.* [S0021-3640(97)00109-6]

PACS numbers: 12.39.Ki

1. In a recent paper[1] it was shown that the effective action of the gluodynamics string obtained from the expansion of the averaged Wilson loop $\langle W(C)\rangle$, written with the use of the non-Abelian Stokes theorem[4,5] and cumulant expansion,[5,6] has the form of a series in powers of T_g/L, where T_g is the correlation length of the vacuum and L is the size of the Wilson loop. Keeping in the cumulant expansion only the lowest bilocal term, which is dominant according to lattice data,[7]

$$\langle W(C)\rangle = \mathrm{tr}\,\exp\Bigg(-\int_S d\sigma_{\mu\nu}(w)\int_S d\sigma_{\lambda\rho}(w') \times\langle F_{\mu\nu}(w)\Phi(w,w')F_{\lambda\rho}(w')\Phi(w',w)\rangle\Bigg),$$

and parametrizing it in the following way:[7,8]

$$\langle F_{\mu\nu}(w)\Phi(w,w')F_{\lambda\rho}(w')\Phi(w',w)\rangle = \frac{\hat{1}}{N_c}\Bigg\{(\delta_{\mu\lambda}\delta_{\nu\rho}-\delta_{\mu\rho}\delta_{\nu\lambda})D\Bigg(\frac{(w-w')^2}{T_g^2}\Bigg) + \frac{1}{2}\Bigg[\frac{\partial}{\partial w_\mu}((w-w')_\lambda\delta_{\nu\rho}-(w-w')_\rho\delta_{\nu\lambda})$$

$$+\frac{\partial}{\partial w_\nu}((w-w')_\rho\delta_{\mu\lambda}-(w-w')_\lambda\delta_{\mu\rho})\Big]D_1\left(\frac{(w-w')^2}{T_g^2}\right)\Big\},$$

where D and D_1 are two renormalization-group invariant coefficient functions, one arrives at the following effective action of the gluodynamics string, induced by the nonperturbative background fields

$$S_{\text{biloc}}=-\ln\langle W(C)\rangle=\sigma\int d^2\xi\sqrt{g}+\frac{1}{\alpha_0}\int d^2\xi\sqrt{g}g^{ab}(\partial_a t_{\mu\nu})(\partial_b t_{\mu\nu})$$
$$+O\left(\frac{T_g^6}{L^2}\alpha_s\text{tr}\langle F_{\mu\nu}^2(0)\rangle\right), \tag{1}$$

where

$$\sigma=4T_g^2\int d^2z D(z^2)$$

is the string tension of the Nambu–Goto term, and

$$\frac{1}{\alpha_0}=\frac{1}{4}T_g^4\int d^2z z^2(2D_1(z^2)-D(z^2))$$

is the inverse bare coupling constant of the rigidity term. Here $\partial_a\equiv\partial/\partial\xi^a$; $a,b=1,2$; $g_{ab}=(\partial_a w_\mu)(\partial_b w_\mu)$ is the induced metric tensor, $g=\det\|g_{ab}\|$, and $t_{\mu\nu}=(1/\sqrt{g})\varepsilon^{ab}(\partial_a w_\mu)(\partial_b w_\nu)$ is the extrinsic curvature of the string world sheet.

The aim of this letter is to apply action (1) to the derivation of the correction to the Hamiltonian of the quark–antiquark system in the confining QCD vacuum, which was obtained in Ref. 2 for the case of equal masses of a quark and antiquark and generalized in Ref. 3 to the case of arbitrary masses. In both Refs. 2 and 3 only the Nambu–Goto term on the right-hand side of Eq. (1) was taken into account in the expression for the Green function of the spinless $q\bar{q}$ system, which, by virtue of the Feynman–Schwinger representation, can be written in the form

$$G(x\bar{x}|y\bar{y})=\int_0^\infty ds\int_0^\infty d\bar{s}\int DzD\bar{z}e^{-K-\bar{K}}\langle W(C)\rangle, \tag{2}$$

where

$$K=m_1^2 s+\frac{1}{4}\int_0^s d\gamma\dot{z}^2(\gamma),\quad \bar{K}=m_2^2\bar{s}+\frac{1}{4}\int_0^{\bar{s}}d\gamma\dot{\bar{z}}^2(\gamma).$$

Our goal here is to take the rigidity term into account as well. In analogy with Ref. 3, we shall consider a $q\bar{q}$ system with arbitrary masses of the quark and antiquark.

In this way we shall work within the same approximations that were used in Refs. 2 and 3, namely, we shall disregard spin effects and the influence of additional quark loops. Secondly, we shall neglect quark trajectories with backward motion in proper time, which might lead to the creation of additional $q\overline{q}$ pairs.

Besides that, we shall use the straight-line approximation for the minimal surface S; this, as was argued in Refs. 2 and 3, corresponds to the valence quark approximation. Such a ''minimal'' string may rotate and oscillate longitudinally. This approximation is inspired by two limiting cases: $l=0$ and $l\to\infty$.

The first case will be then investigated in more detail, and the correction to the Hamiltonian of the relativistic quark model[9] due to the rigidity term in the limit of large masses of the quark and antiquark will be derived.

The main results of this letter are summarized in the Conclusion.

2. RIGIDITY CORRECTION TO THE HAMILTONIAN OF THE ''MINIMAL'' QCD STRING WITH SPINLESS QUARKS

Making use of the auxiliary field formalism,[2,10] one can represent the Green function (2) with $\langle W(C)\rangle$ defined via Eq. (1) in the following way:

$$G(x\overline{x}|y\overline{y})=\int D\mathbf{z}D\overline{\mathbf{z}}D\mu_1 D\mu_2 Dh_{ab}\exp(-K'-\overline{K'})$$
$$\times\exp\left[(-\sigma+2\overline{\alpha})\int d^2\xi\sqrt{h}\right]\exp\left[-\overline{\alpha}\int d^2\xi\sqrt{h}h^{ab}(\partial_a w_\mu)(\partial_b w_\mu)\right.$$
$$\left.-\frac{1}{\alpha_0}\int d^2\xi\sqrt{h}h^{ab}(\partial_a t_{\mu\nu})(\partial_b t_{\mu\nu})\right], \tag{3}$$

where we have integrated over the Lagrange multiplier $\lambda^{ab}(\xi)=\alpha(\xi)h^{ab}(\xi)+f^{ab}(\xi)$, $f^{ab}h_{ab}=0$, and $\overline{\alpha}$ is the mean value of $\alpha(\xi)$. Here $t_{\mu\nu}=(1/\sqrt{h})\,\varepsilon^{ab}(\partial_a w_\mu)\times(\partial_b w_\nu)$,

$$K'+\overline{K'}=\frac{1}{2}\int_0^T d\tau\left[\frac{m_1^2}{\mu_1(\tau)}+\mu_1(\tau)(1+\dot{\mathbf{z}}^2(\tau))+\frac{m_2^2}{\mu_2(\tau)}+\mu_2(\tau)(1+\dot{\overline{\mathbf{z}}}^2(\tau))\right], \tag{4}$$

$$T=\frac{1}{2}(x_0+\overline{x}_0-y_0-\overline{y}_0),\quad \mu_1(\tau)=\frac{T}{2s}\dot{z}_0(\tau),\quad \mu_2(\tau)=\frac{T}{2s}\dot{\overline{z}}_0(\tau),$$

and the no-backtracking-time approximation[2,3]

$$\mu_1(\tau)>0,\quad \mu_2(\tau)>0 \tag{5}$$

was used. As in Refs. 2 and 3 we use in the valence quark sector (5) the approximation that the minimal surface S may be parametrized by the straight lines connecting points $z_\mu(\tau)$ and $\overline{z}_\mu(\tau)$ with the same τ, i.e., the trajectories of a quark and antiquark are synchronized: $z_\mu=(\tau,\mathbf{z})$, $\overline{z}_\mu=(\tau,\overline{\mathbf{z}})$, $w_\mu(\tau,\beta)=\beta z_\mu(\tau)+(1-\beta)\overline{z}_\mu(\tau)$, $0\leqslant\beta\leqslant 1$.

Introducing the auxiliary fields[2]

$$\nu(\tau,\beta)=T\sigma\frac{h_{22}}{\sqrt{h}},\quad \eta(\tau,\beta)=\frac{1}{T}\frac{h_{12}}{h_{22}}$$

and making a rescaling

$$z_\mu\to\sqrt{\frac{\sigma}{2\overline{\alpha}}}z_\mu,\quad \overline{z}_\mu\to\sqrt{\frac{\sigma}{2\overline{\alpha}}}\overline{z}_\mu$$

one obtains from the last exponential function on the right-hand side of Eq. (3) the following action of the string without quarks:

$$A_{\rm str}=\int_0^T d\tau\int_0^1 d\beta\frac{\nu}{2}\Bigg\{\dot{w}^2+\left(\left(\frac{\sigma}{\nu}\right)^2+\eta^2\right)r^2-2\eta(\dot{w}r)+\frac{\sigma T^2}{\alpha_0\overline{\alpha^2}}\frac{1}{h}\Big[\ddot{w}^2r^2-(\ddot{w}r)^2$$
$$+\dot{w}^2\dot{r}^2-(\dot{w}\dot{r})^2+2((\ddot{w}\dot{w})(\dot{r}r)-(\ddot{w}\dot{r})(\dot{w}r))+\left(\left(\frac{\sigma}{\nu}\right)^2+\eta^2\right)(\dot{r}^2r^2-(\dot{r}r)^2)$$
$$-2\eta((\ddot{w}\dot{r})r^2-(\ddot{w}r)(\dot{r}r)+(\dot{w}\dot{r})(\dot{r}r)-(\dot{w}r)\dot{r}^2)\Big]\Bigg\},\qquad(6)$$

where a dot stands for $\partial/\partial\tau$, $r_\mu(\tau)=z_\mu(\tau)-\overline{z}_\mu(\tau)$ is the relative coordinate, and as in Ref.1, we have assumed that the string world sheet is not very crumpled, so that h_{ab} is a smooth function.

Let us now introduce the center-of-mass coordinate $R_\mu(\tau)=\zeta(\tau)z_\mu(\tau)+(1-\zeta(\tau))\overline{z}_\mu(\tau)$, where $\zeta(\tau)\equiv\zeta_1(\tau)+(1/\alpha_0)\zeta_2(\tau)$, $0\leqslant\zeta(\tau)\leqslant1$ should be determined from the requirement that $\dot{R}_\mu$ decouples from $\dot{r}_\mu$.[3] Next, assuming that a meson as a whole moves with a constant speed (which is true for a free meson), i.e., $\ddot{R}=0$, and bringing together the quark kinetic terms (4) and pure string action (6), we arrive at the following action of the QCD string with quarks

$$A=\int_0^T d\tau\Bigg\{\frac{m_1^2}{2\mu_1}+\frac{m_2^2}{2\mu_2}+\frac{\mu_1}{2}+\frac{\mu_2}{2}+\frac{1}{2}\left(\mu_1+\mu_2+\int_0^1 d\beta\nu\right)\dot{R}^2+\Bigg(\mu_1(1-\zeta_1)$$
$$-\mu_2\zeta_1+\int_0^1 d\beta(\beta-\zeta_1)\nu\Bigg)(\dot{R}\dot{r})-\int_0^1 d\beta\nu\eta(\dot{R}r)+\int_0^1 d\beta(\zeta_1-\beta)\eta\nu(\dot{r}r)$$
$$+\frac{1}{2}\left(\mu_1(1-\zeta_1)^2+\mu_2\zeta_1^2+\int_0^1 d\beta(\beta-\zeta_1)^2\nu\right)\dot{r}^2+\frac{1}{2}\int_0^1 d\beta\left(\frac{\sigma^2}{\nu}+\eta^2\nu\right)r^2$$
$$+\frac{1}{\alpha_0}\Big[\zeta_2(\mu_1(\zeta_1-1)+\mu_2\zeta_1)\dot{r}^2-\zeta_2(\mu_1+\mu_2)(\dot{R}\dot{r})+\int_0^1 d\beta\nu\Big(\zeta_2(\zeta_1-\beta)\dot{r}^2$$
$$-\zeta_2(\dot{R}\dot{r})+\zeta_2\eta(\dot{r}r)+\frac{1}{2}(\beta-\zeta_1)^2[\ddot{\mathbf{r}},\mathbf{r}]^2+\frac{1}{2}\dot{R}^2\dot{r}^2-\frac{1}{2}(\dot{R}\dot{r})^2+(\beta-\zeta_1)((\ddot{r}\dot{R})(\dot{r}r)$$

$$-(\ddot{r}\dot{r})(\dot{R}r))+\frac{1}{2}\left(\left(\frac{\sigma}{\nu}\right)^2+\eta^2\right)[\dot{\mathbf{r}},\mathbf{r}]^2+\eta((\beta-\zeta_1)((\ddot{r}r)(\dot{r}r)-(\ddot{r}\dot{r})r^2)+(\dot{R}r)\dot{r}^2$$

$$-(\dot{R}\dot{r})(\dot{r}r))\Bigg)\Bigg]\Bigg\}, \tag{7}$$

where we have performed a rescaling

$$z_\mu\to\overline{\alpha}\sqrt{\frac{h}{\sigma T^2}}z_\mu, \quad \overline{z}_\mu\to\overline{\alpha}\sqrt{\frac{h}{\sigma T^2}}\overline{z}_\mu, \quad \nu\to\frac{\sigma T^2}{\overline{\alpha}^2 h}\nu.$$

Integrating over η, one gets in the zeroth order in $1/\alpha_0$

$$\eta_{\text{ext}}=\frac{(\dot{r}r)}{r^2}\left(\beta-\frac{\mu_1}{\mu_1+\mu_2}\right),$$

which, together with the condition $\dot{R}\dot{r}=0$, yields

$$\zeta_2^{\text{ext}}=\frac{(\dot{r}r)^2}{r^2}\,\frac{\dfrac{\mu_1}{\mu_1+\mu_2}\displaystyle\int_0^1 d\beta\nu-\int_0^1 d\beta\beta\nu}{\mu_1+\mu_2+\displaystyle\int_0^1 d\beta\nu},$$

while $\zeta_1^{\text{ext}}=[\mu_1+\int_0^1 d\beta\beta\nu]/[\mu_1+\mu_2+\int_0^1 d\beta\nu]$ was found in Ref. 3.

Finally, in order to obtain the desirable Hamiltonian, we shall perform the usual canonical transformation from $\dot{\mathbf{R}}$ to the total momentum $\mathbf{P}$ in the Minkowski space–time:

$$\int D\mathbf{R}\,\exp\left[i\int L(\dot{\mathbf{R}},\dots)d\tau\right]=\int D\mathbf{R}D\mathbf{P}\,\exp\left[i\int(\mathbf{P}\cdot\dot{\mathbf{R}}-H(\mathbf{P},\dots))d\tau\right],$$

where $H(\mathbf{P},\dots)=\mathbf{P}\cdot\dot{\mathbf{R}}-L(\dot{\mathbf{R}},\dots)$, and choose the meson rest frame as $\mathbf{P}=\partial L(\dot{\mathbf{R}},\dots)/\partial\dot{\mathbf{R}}=0$. After performing the transformation from $\dot{\mathbf{r}}$ to $\mathbf{p}$ we get the following Hamiltonian:

$$H=H^{(0)}+\frac{1}{\alpha_0}H^{(1)}. \tag{8}$$

Here

$$H^{(0)}=\frac{1}{2}\left[\frac{(\mathbf{p}_r^2+m_1^2)}{\mu_1}+\frac{(\mathbf{p}_r^2+m_2^2)}{\mu_2}+\mu_1+\mu_2+\sigma^2\mathbf{r}^2\int_0^1\frac{d\beta}{\nu}+\nu_0+\frac{\mathbf{L}^2}{\rho\mathbf{r}^2}\right] \tag{9}$$

with

$$\rho=\mu_1+\nu_2-\frac{(\mu_1+\nu_1)^2}{\mu_1+\mu_2+\nu_0}, \quad \nu_i\equiv\int_0^1 d\beta\beta^i\nu, \quad \mathbf{p}_r^2\equiv\frac{(\mathbf{p}\cdot\mathbf{r})^2}{\mathbf{r}^2}, \quad \mathbf{L}\equiv[\mathbf{r},\mathbf{p}]$$

is the Hamiltonian of the ''minimal'' Nambu—Goto string with quarks, which was derived and investigated in Ref. 3, while the new Hamiltonian $H^{(1)}$ has the form

$$H^{(1)}=\frac{a_1}{\rho^2}\mathbf{L}^2+\frac{a_2}{\rho^2}\dot{\mathbf{L}}^2+\frac{a_3}{2\tilde{\mu}^3}|\mathbf{r}|(\mathbf{p}_r^2)^{\frac{3}{2}}+\frac{a_4}{\tilde{\mu}^4}(\mathbf{p}_r^2)^2+\frac{a_5}{2\tilde{\mu}\rho^2}\frac{\sqrt{\mathbf{p}_r^2\mathbf{L}^2}}{|\mathbf{r}|}+\frac{a_6}{2\tilde{\mu}^2\rho^2}\frac{\mathbf{p}_r^2\mathbf{L}^2}{\mathbf{r}^2}, \tag{10}$$

where $\tilde{\mu}=\mu_1\mu_2/\mu_1+\mu_2$, and the coefficients $a_k, k=1,\ldots,6$ read as follows:

$$a_1=\frac{\sigma^2}{2}\int_0^1\frac{d\beta}{\nu},\quad a_2=\frac{1}{2}\left[\nu_2+\frac{(\mu_1+\nu_1)(\nu_0(\mu_1-\nu_1)-2\nu_1(\mu_1+\mu_2))}{(\mu_1+\mu_2+\nu_0)^2}\right],$$

$$a_3=3\frac{\dot{\tilde{\mu}}}{\tilde{\mu}}B-\dot{B},$$

$$a_4=\frac{1}{2(\mu_1+\mu_2)(\mu_1+\mu_2+\nu_0)}\left[\frac{\nu_0(\mu_1\nu_0-\nu_1(\mu_1+\mu_2))^2}{(\mu_1+\mu_2)(\mu_1+\mu_2+\nu_0)}-\nu_1(\mu_1+\mu_2)(\nu_1-2\mu_2)\right.$$
$$\left.-\mu_1\nu_0(\mu_1+2\mu_2)\right],$$

$$a_5=\frac{\dot{\tilde{\mu}}}{\tilde{\mu}}B-\dot{B},\quad a_6=\nu_2+\frac{\nu_1^2+2\mu_1\nu_0-2\mu_2\nu_1}{\mu_1+\mu_2+\nu_0}$$
$$+\frac{1}{\mu_1+\mu_2}\left[\frac{1}{\mu_1+\mu_2}\left(\frac{(\mu_1\nu_0-\nu_1(\mu_1+\mu_2))^2(3\nu_0+2(\mu_1+\mu_2))}{(\mu_1+\mu_2+\nu_0)^2}+\mu_1(\mu_1\nu_0\right.\right.$$
$$\left.\left.-2\nu_1(\mu_1+\mu_2))\right)-\frac{\mu_1^2\nu_0}{\mu_1+\mu_2+\nu_0}\right],$$

$$B\equiv\frac{\nu_1(\mu_1+\mu_2)(\nu_1-2\mu_2)+\mu_1\nu_0(\mu_1+2\mu_2)}{(\mu_1+\mu_2)(\mu_1+\mu_2+\nu_0)}.$$

During the derivation of $H^{(1)}$ we have placed the origin at the center of mass of the initial state, so that $\dot{\mathbf{R}}\cdot\dot{\mathbf{r}}\ll 1$, and the term

$$-\frac{1}{2\alpha_0}\int_0^T d\tau\nu_0(\dot{\mathbf{R}}\cdot\dot{\mathbf{r}})^2$$

on the right-hand side of Eq. (7) has been neglected.

Notice that Hamiltonian (8)–(10) contains auxiliary fields μ_1, μ_2, and ν. In order to construct the Hamiltonian operator that acts on wave functions, one must integrate over these fields (this implies a substitution of their extremal values, which could be obtained from the corresponding saddle-point equations, into Eqs. (8)–(10)) and perform Weil ordering.[11]

Let us now apply Hamiltonian (10) to the derivation of the rigid-string correction to the Hamiltonian of the so-called relativistic quark model,[9] i.e., consider the case when the orbital momentum is equal to zero. In what follows we shall for simplicity put the mass

of a quark equal to the mass of an antiquark: $m_1=m_2\equiv m$. In order to get $H^{(1)}$, one should substitute the extremal values of the fields μ_1, μ_2, and ν of the zeroth order in $1/\alpha_0$, $\mu_1^{\rm ext}=\mu_2^{\rm ext}=\sqrt{\mathbf{p}^2+m^2}$ and $\nu_{\rm ext}=\sigma|\mathbf{r}|$, into Eq. (10). The limit of large masses of a quark and antiquark means that $m\gg\sqrt{\sigma}$. In this case we obtain from Eq. (10) the rigid-string Hamiltonian $H^{(1)}=-(4\sigma|\mathbf{r}|/m^4)(\mathbf{p}_r^2)^2$ and then, from Eqs. (8) and (9), the following expression for the total Hamiltonian

$$H=2m+\sigma|\mathbf{r}|+\frac{\mathbf{p}^2}{m}-\left(\frac{1}{4m^3}+\frac{4\sigma|r|}{\alpha_0 m^4}\right)(\mathbf{p}^2)^2. \tag{11}$$

3. In this letter we have derived a correction to the Hamiltonian (9) of the QCD string with spinless quarks, which was found in Ref. 3; this correction, which arises from the rigidity term in the gluodynamics string effective action,[1] is given by formula (10). The Hamiltonian obtained contains corrections to the orbital momentum of the system and also several operators of higher than second order in the momentum. The latter corrections arise as a consequence of the fact that the rigid-string theory is a theory with higher derivatives.

We have used the Hamiltonian obtained to derive the rigid-string contribution to the Hamiltonian of the relativistic quark model in the case of equal large masses of a quark and antiquark, so that the total Hamiltonian is given by formula (11).

I am grateful to Professors M. G. Schmidt and Yu. A. Simonov for helpful discussions. I would also like to thank the theory group of the Quantum Field Theory Department of the Institut für Physik of the Humboldt-Universität of Berlin for kind hospitality.

[1] D. V. Antonov, D. Ebert and Yu. A. Simonov, Mod. Phys. Lett. A **11**, 1905 (1996).
[2] A. Yu. Dubin, A. B. Kaidalov and Yu. A. Simonov, Yad. Fiz. **56**, 213 (1993) [Phys. At. Nucl. **56**, 1745 (1993)]; Phys. Lett. B **323**, 41 (1994).
[3] E. L. Gubankova and A. Yu. Dubin, Phys. Lett. B **334**, 180 (1994), preprint ITEP 62-94.
[4] M. B. Halpern, Phys. Rev. D **19**, 517 (1979); I. Ya. Aref'eva, Theor. Math. Phys. **43**, 111 (1980); N. Bralic, Phys. Rev. D **22**, 3090 (1980).
[5] Yu. A. Simonov, Yad. Fiz. **50**, 213 (1989) [Sov. J. Nucl. Phys. **50**, 134 (1989)].
[6] N. G. Van Kampen, *Stochastic Processes in Physics and Chemistry*, North-Holland Physics Publishing, 1984.
[7] Yu. A. Simonov, Yad. Fiz. **54**, 192 (1991) [Sov. J. Nucl. Phys. **54**, 115 (1991)].
[8] H. G. Dosch, Phys. Lett. B **190**, 177 (1987); Yu. A. Simonov, Nucl. Phys. B **307**, 512 (1988); H. G. Dosch and Yu. A. Simonov, Phys. Lett. B **205**, 339 (1988); Z. Phys. C **45**, 147 (1989); Yu. A. Simonov, Nucl. Phys. B **324**, 67 (1989); Phys. Lett. B **226**, 151 (1989); Phys. Lett. B **228**, 413 (1989).
[9] P. Cea, G. Nardulli and G. Preparata, Z. Phys. C **16**, 135 (1982); Phys. Lett. B **115**, 310 (1982); J. Carlson *et al.*, Phys. Rev. D **27**, 233 (1983); J. L. Basdevant and S. Boukraa, Z. Phys. C **30**, 103 (1986); S. Godfrey and N. Isgur, Phys. Rev. D **32**, 189 (1985).
[10] A. M. Polyakov, *Gauge Fields and Strings*, Harwood, 1987.
[11] T. D. Lee, *Particle Physics and Introduction to Field Theory*, Harwood, 1990.

Published in English in the original Russian journal. Edited by Steve Torstveit.

Dominant role of dielectronic satellites in the radiation spectra of a laser plasma near the target surface

F. B. Rosmey
University of Bohemia, Institute of Experimental Physics V, D-44780 Bohemia, Germany

A. Ya. Faenov, T. A. Pikuz, and I. Yu. Skobelev
Main Science Center — All-Russia Scientific-Research Institute of Physicotechnical and Radio Engineering Measurements, 141570 Mendeleevo, Moscow Region, Russia

A. E. Stepanov, A. N. Starostin, V. S. Rerikh, and V. A. Makhrov
TRINITI, 142092 Troitsk, Moscow District, Russia

F. Flora, S. Bollanti, P. Di Lazzaro, T. Letardi, K. Vigli-Papadaki, and A. Nottola
ENEA, Dipartimento Innovazione, 00044 Frascati, Rome, Italy

A. Grilli
INFN Frascati, 00044 Frascati, Rome, Italy

L. Palladino and A. Reale
Dipatamento di Fisica e INFN g. e. LNGS, Universita de L'Aquila, 67010 L'Aquila, Italy

A. Scafati and L. Reale
Instituto Sup. Di Sanita, Roma e INFN cez Sanita, 00040 Rome, Italy

(Submitted 31 March 1997)
Pis'ma Zh. Éksp. Teor. Fiz. **65**, No. 9, 679–684 (10 May 1997)

It is shown that in a dense, not very hot, multiply charged plasma the satellite structures of resonance lines can become more intense than the resonance lines themselves. Experimental and theoretical investigations show that the conditions under which the satellite structures dominate in the emission spectrum of the plasma are quite easily realized experimentally and, furthermore, apparently they will be the most typical case in investigations of compressed plasma regions in inertial-confinement fusion experiments and in the study of plasma produced by high-contrast pico- and femtosecond laser pulses. © *1997 American Institute of Physics.* [S0021-3640(97)00209-0]

PACS numbers: 52.25.Nr, 52.70.La, 52.58.Hm

X-ray spectral diagnostics methods have long been used, very successfully, for determining the parameters of both laboratory and astrophysical plasmas. For example, they have been used to obtain extensive information on the ablation plasma in inertial confinement fusion (ICF) experiments and there are plans to use them for diagnostics of compressed regions in thermonuclear targets in large-scale ICF experiments (see, for example, Refs. 1–3).

Many existing x-ray spectral diagnostics methods are based on the detection of the

resonance lines of multiply charged H- and He-like ions, i.e., $2p-1s$ and $1s2p-1s^2$ transitions, respectively. However, these resonance lines are bordered by satellite structures due to transitions of the type $2pnl-1snl$ and $1s2pnl-1s^2nl$ in ions with a smaller charge. For $n=2$ the satellites lie quite far away from the corresponding resonance lines, whereas for $n\geqslant 3$ the splitting becomes very small, and many of these satellite lines lie within the contour of the resonance line. This means that, strictly speaking, experiments all record not a single resonance line but rather the sum of the resonance line with the corresponding satellites. This circumstance ordinarily does not create additional difficulties, since in the most common case of a quite hot plasma which is not too dense, the intensity of satellite structures with $n\geqslant 3$ is in general quite low. Moreover, it drops rapidly with increasing n, and the contribution of the satellites to the resonance line does not exceed $\sim 10\%$. However, it should be remembered that the intensities of the satellites and the resonance lines themselves depend differently on both the ion charge Z and plasma parameters, such as the temperature T_e, the density N_e, and the linear size L of the plasma: The relative intensity of the satellite structures increases with increasing Z, decreasing T_e, and increasing N_e and L. The first two dependences are quite obvious (see, for example, Refs. 4 and 5). The dependence on N_e appears as a result of both the additional filling of doubly degenerate states with small autoionization constants and a decrease in the intensity of the resonance line due to self-absorption, and the dependence on L is due completely to self-absorption. Therefore, satellite structures in a dense, not very hot, multiply charged plasma can become more intense than the resonance lines themselves, and it may be impossible to record the resonance lines. This conclusion by itself is very obvious, and the real question is whether or not the conditions for realizing such a situation are too exotic. Answering this question is our objective in the present work. Our experimental and theoretical investigations showed that the conditions under which the satellite structures dominate the radiation spectrum of a plasma are quite easily realized experimentally and furthermore they apparently will be the most typical case in investigations of compressed plasma regions in ICF experiments and in the study of plasma produced by high-contrast pico- and femtosecond laser pulses, i.e., in investigations which are of greatest interest today.

The experimental investigations were performed on the Hercules device (Frascati), which consists of a XeCl laser with an active-medium volume of $9\times 4\times 100$ cm, wavelength $\lambda=308$ nm, pulse energy 2 J, and pulse duration 12 ns. The radiation was focused into a 40–70 μm in diameter spot on the surface of a solid magnesium target, so that the flux density was equal to $(4-8)\cdot 10^{12}$ W/cm^2. The laser operated in the periodic-pulse mode with a repetition frequency of 10 Hz. The spectrum was ordinarily obtained over 20–40 shots; the target was moved after each shot.

The soft x-ray radiation from the plasma was recorded with a spherically curved mica crystal spectrograph.[6–8] The FSPR-1 arrangement[7] of the crystal (radius of curvature 186 mm), the plasma, and the photographic film made it possible to obtain spectra with a high spectral resolution $\lambda/\Delta\lambda\approx 10000$ and a spatial resolution $\delta x\approx 20$ μm in the direction of expansion of the plasma. The recorded spectral range of 9.1–9.35 Å contained the resonance line (W) $1s2p\,^1P_1-1s^2\,^1S_0$ and the intercombination line (Y) $1s2p\,^3P_1-1s^2\,^1S_0$ of the He-like ion Mg XI and the satellite structures due to the radiative transitions $1s2lnl'-1s^2nl'$ from the twofold degenerate states of the Li-like ion

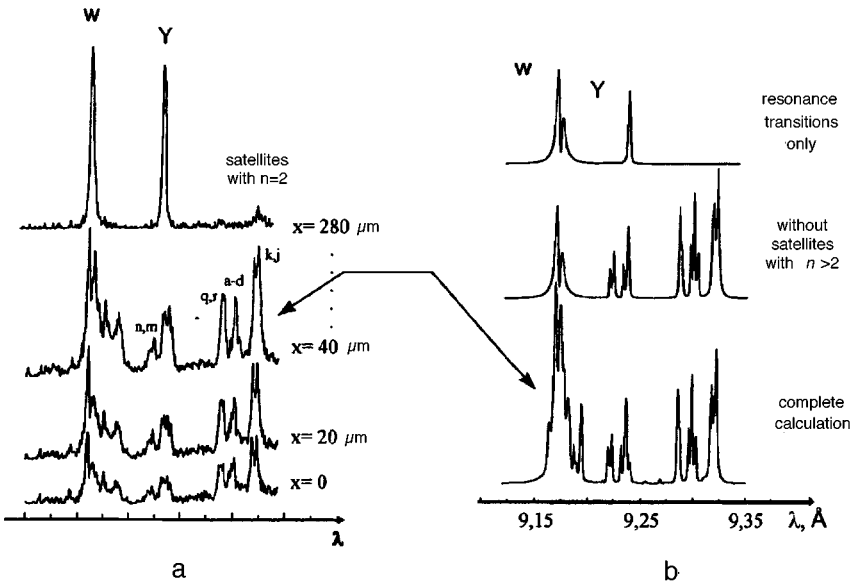

FIG. 1. a) Radiation spectra of a magnesium laser plasma. The spectra correspond to plasma regions located at distances $x=0-280$ μm from the target surface. The standard designations are used for satellites with $n=2$: $q,r,\ldots$ (see, for example, Ref. 5), W and Y are resonance and intercombination lines of the MgXI ion. b) Theoretical modeling results for the radiation spectrum of a plasma from the region $x=40$ μm. The model spectrum was constructed for $N_e=10^{21}$ cm^{-3}, $T_e=80$ eV, and $L=50$ μm.

MgX. Examples of densitometer traces of spectra corresponding to plasma regions located at different distances from the target surface are displayed in Fig. 1a.

It is evident from Fig. 1a that at sufficiently large distances from the target surface ($x>100$ μm) the radiation spectrum of the plasma looks to be very standard: The W and Y lines dominate the spectrum, and the total radiation energy in the satellite structures is very low. The situation changes qualitatively as the target is approached: 1) The well-known satellites q, r, $a-d$, k, and j become at least as intense as the resonance line, 2) intense satellites appear near the intercombination line, and 3) the contour of the resonance line becomes strongly asymmetric, with spectral lines clearly observed on its long-wavelength wing. We used the ''Maria'' kinetic code[9] to model this situation theoretically. This code represents a nonstationary, multilevel, radiation–collisional model with self-absorption taken into account in the leakage-factor approximation. An important feature of the Maria code is that a large number of autoionizing states of ions of different charges are included in the calculation. For example, for the Li-like MgX ion all states of the $1s2lnl'$ configurations with $2\leqslant n\leqslant 7$ were included in the present work. The calculations were performed for a large set of values of the plasma parameters and made it possible to investigate the dependence of the emission spectrum on the plasma density, temperature, and size. Figure 2 displays as an example the most nontrivial, in our opinion, dependence of the spectrum on the linear size of the plasma for fixed values of the plasma density $N_e=10^{21}$ cm^{-3} and temperature $T_e=80$ eV.

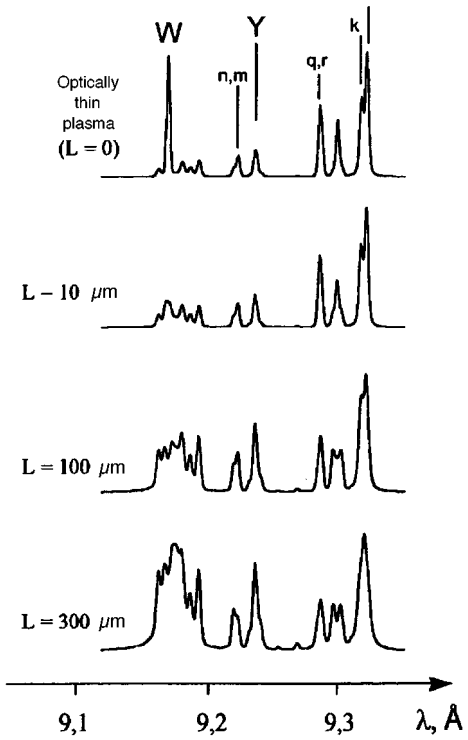

FIG. 2. Computational results for the emission spectrum of a magnesium plasma in the region 9.1–9.4 Å for $N_e = 10^{21}$ cm^{-3}, $T_e = T_i = 80$ eV, and different geometric dimensions of the plasma object.

One can see from Fig. 2 that the form of the radiation spectrum for an optically thin plasma is qualitatively different from that of an optically thick plasma (in the case $L = 300$ μm, for example, the optical thickness of the plasma at the center of a resonance line is $\tau_0(W) \sim 500$). As the plasma increases in size, at first self-absorption appears in the resonance lines, while the satellite lines remain practically unchanged (see the spectrum for $L = 10$ μm and also Refs. 10 and 11). For $L = 100$ μm the plasma becomes optically thick even for satellites with $n = 2$. Since a strong nonradiative decay channel (autoionization) exists for the autoionizing levels, imprisonment of the radiation strongly affects the satellite intensities even for $\tau \sim 1$ (see, for example, Refs. 12–14). As a result, satellites with $n > 2$ play a relatively large role in the radiation spectrum of the plasma. For $L = 300$ μm the optical thickness of the plasma reaches 1 even for satellites with $n = 3$. Therefore, as the plasma size increases, satellite structures with large $n > 3$, which are concentrated close to the resonance line, start to play an increasingly important role. As a result, a complex ''resonance structure'' forms at the location of the resonance line, and the resonance line itself makes only a very small contribution to this structure (see the $L = 300$ μm spectrum in Fig. 2).

The kinetic calculations made it possible to describe the observed spectra quite well. For example, Fig. 1b shows the modeling results for the spectrum emitted from a region

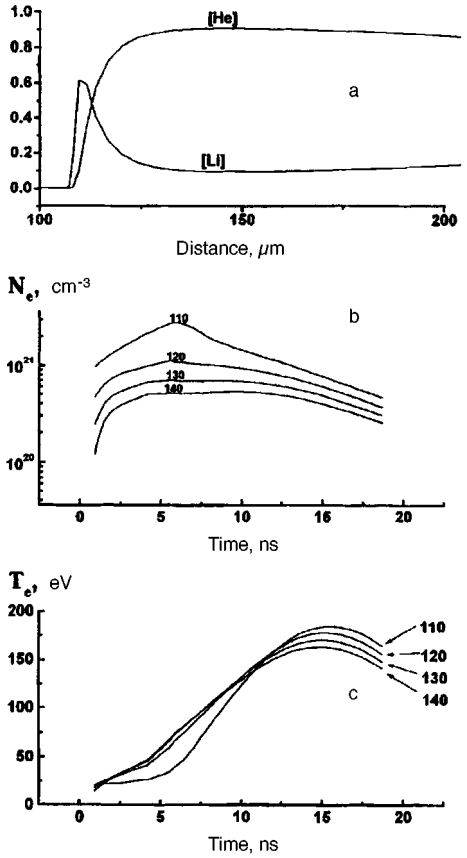

FIG. 3. Relative densities of Li- and He-like Mg ions at time $t=7.1$ ns, corresponding to the maximum distance of the critical surface from the target, as a function of the radius (a) and the time dependence of the electron density (b) and temperature (c) for a number of distances r from the center of the spherical surface of the target. The numbers on the curves correspond to the values of the radius r in microns. Since the initial target radius was equal to 100 μm, the quantity $x=r-100$ μm gives the distance from the target surface.

of the plasma located at a distance $x=40$ μm from the target (the parameters of the model spectrum are given in the figure caption). From this figure it is also clear that the complicated ''resonance structure'' is formed by satellites with $n>2$. We note that the theoretical spectrum shown in Fig. 1b was constructed taking into account the inhomogeneous Doppler shift of the spectrum, due to the macroscopic motion of the plasma, and the presence of a small number $(6\cdot 10^{-5})$ of high-energy electrons ($E\sim 1$ keV, see also Ref. 9).

The good agreement between the observed and computed radiation spectra shows that near the surface the plasma temperature was quite low (~ 80 eV) and the plasma density was quite high ($\sim 10^{21}$ cm^{-3}) under the experimental conditions of the present work. This conclusion also follows from the gas-dynamic calculations which we performed using the Hydra code.[15] The calculations were performed in a one-dimensional

spherical geometry. The initial target radius was set equal to 100 μm. The temporal form of the laser pulse was Gaussian with a width of 14.4 ns at half height. The peak density of the laser radiation flux, scaled to the initial radius of the target, was equal to $3 \cdot 10^{12}$ W/cm^2. The calculation started 14.4 ns before the peak of the laser pulse. Together with the gas-dynamic equations, the equations governing the population kinetics of the levels of Mg ions with all charge multiplicities (from neutrals to bare nuclei) were solved self-consistently. The radiation energy losses and reabsorption of radiation in the spectral lines were taken into account in the photon-escape-probability approximation. Some of the computed curves are presented in Fig. 3. We note that, as one can see from Fig. 3a, a large number of Li-like ions is present in the plasma near the target; this increases the excitation efficiency of satellites with $n>2$ from the $1s^2nl$ states upon the direct excitation of an inner $1s$ electron.

For other laser pulse parameters characteristic for most of the experiments performed with laser plasmas over the last two decades ($\lambda = 1.06$ μm, $\tau = 1$ ns, $q = 10^{14}$ W/cm^2), regions of comparatively cold, dense plasma should also exist near the target. However, these regions will be much smaller, and in spectra recorded with the ordinarily realizable spatial resolution $\delta x \geqslant 100$ μm they will not be noticeable. Inadequate spectral resolution has a similar effect: The complicated ''resonance structure'' will appear as a single line with a smooth contour. The satellite dominance which we observed in the emission spectrum of a laser plasma in the present work will apparently be even more important in experiments on femtosecond heating of plasma by high-contrast pulses, where, as a result of the high (solid-state) density of the plasma produced, the ionization-state composition will shift in the direction of lower states of ionization, and satellite structures due to the radiative decay of autoionizing states with two highly excited electrons in Be-, B-, ...-like ions will play a large role.

[1] A. A. Hammer, N. D. Delamater, and Z. M. Koenig, Laser Part. Beams **9**, 3 (1991).
[2] R. S. Marjoribanks, F. Budnik, G. Kulcsar, and L. Zhao, Rev. Sci. Instrum. **66**, 683 (1995).
[3] C. A. Back, S. H. Glenzer, R. W. Lee *et al.*, *Atomic Processes in Plasmas, 10th Topical Conference*, San Francisco, January 1996, AIP Press, New York, 1996, p. 123.
[4] L. A. Vaĭnshteĭn, I. I. Sobel'man, and E. A. Yukov, *Excitation of Atoms and Spectral Line Broadening* [in Russian], Nauka, Moscow, 1979.
[5] V. A. Boiko, A. V. Vinogradov, S. A. Pikuz *et al.*, *X-Ray Spectroscopy of Laser Plasma* [in Russian], VINITI, Moscow, 1980; J. Sov. Laser Research **6**, 81 (1985).
[6] A. Ya. Faenov, S. A. Pikuz, A. I. Erko *et al.*, Phys. Scr. **50**, 333 (1994).
[7] I. Yu. Skobelev, A. Ya. Faenov, B. A. Bryunetkin *et al.*, Zh. Eksp. Teor. Fiz. **108**, 1263 (1995) [JETP **81**, 692 (1995)].
[8] T. A. Pikuz, A. Ya. Faenov, S. A. Pikuz *et al.*, J. X-Ray Sci. Technol. **5**, 323 (1995).
[9] F. B. Rosmey, A. Ya. Faenov, T. A. Pikuz *et al.*, J. Quant. Spectrosc. Radiat. Transfer (1997), in press.
[10] Y. Aglitskiy, T. Lehecka, A. Denis *et al.*, Phys. Plasmas **3**, 3438 (1996).
[11] Y. Aglitskiy, T. Lehecka, A. Denis *et al.*, Rev. Sci. Instrum. **68**, 806 (1997).
[12] V. A. Boĭko, S. A. Maĭorov, S. A. Pikuz *et al.*, Opt. Spektrosk. **52**, 433 (1982) [Opt. Spectrosc. **52**, 259 (1982)].
[13] A. Ya. Faenov, S. A. Pikuz, D. A. Hammer *et al.*, Phys. Rev. A **49**, 3450 (1994).
[14] S. Kienle, F. B. Rosmey, and H. Schmidt, J. Phys. B **28**, 3675 (1995).
[15] A. E. Stepanov, A. N. Starostin, V. C. Roerich *et al.*, J. Quant. Spectrosc. Radiat. Transfer (1997), in press.

Translated by M. E. Alferieff

Simulation of the formation of porous-silicon structures

L. N. Aleksandrov[a)] and P. L. Novikov

Institute of Semiconductor Physics, Siberian Branch of the Russian Academy of Sciences, 630090 Novosibirsk, Russia

(Submitted 24 March 1997)
Pis'ma Zh. Éksp. Teor. Fiz. **65**, No. 9, 685–690 (10 May 1997)

The formation of porous silicon is investigated by the Monte Carlo method in a model that takes account of the nonuniformity of the charge distribution over the silicon–electrolyte interface, hole diffusion, generation, and recombination processes, and size quantization. The structures obtained in a computer simulation for various doping levels of the crystalline substrate, temperatures, HF concentrations, and anode current densities are presented. Analysis of nanoporous structures shows that the porosity depends on the depth and reveals the presence of a fractal dimensionality on scales of less than 10 nm. [S0021-3640(97)00309-5]

PACS numbers: 61.43.Dq, 61.43.Bn

Porous silicon obtained by anodization in a solution of HF has become a promising material for producing electronic devices on account of its visible-range luminescence,[1] its extremely extended surface, and its extensive technological possibilities.[2–4] It is also an interesting object for fundamental investigations, since its fractal structure exhibits a number of optical, diffusion, thermodynamic, and transport properties[5] which have not been completely explained. The mechanism leading to the formation of porous layers is also in dispute.

Together with experimental methods, computer simulation is also used to study the mechanism leading to the formation of porous silicon. All physical models employed are based on the idea that the elementary event contributing to the decomposition of a crystal during anodic etching is an electrochemical reaction with transport of several positive elementary charges (holes) from the crystal into the electrolyte. A model which incorporates diffusion transport of holes to the boundary of the silicon anode (diffusion-limited model) makes it possible to obtain structures which are visually similar to the experimental structures.[6–11] The qualitative dependence of the structure on the anodic current density emerges when hole drift near pore tips is included in the simulation. However, these models do not give detailed agreement between the computed and the real experimental structures (including the pore diameter, the average interpore distance, and so on) or an adequate dependence of the topological characteristics of the modeled structures on the experimental conditions.

In the present work we performed a numerical simulation that makes it possible to follow the formation of porous silicon as a function of the doping level in *p*-Si, the anodic current density, the temperature, and the HF concentration. Hole diffusion, drift, generation, and recombination in the crystal, the formation of a space-charge region (SCR) at

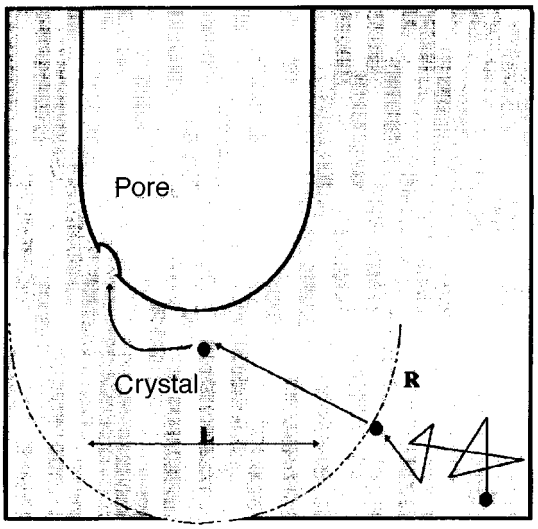

FIG. 1. Diagram illustrating the computational algorithm for p^+-Si.

the pore tips and near the crystal–electrolyte interface, as well as size quantization in nanoparticles are incorporated in the model as processes leading to the formation of porous silicon. All conditions together determine which process dominates. The simulation was performed on both square and cubic meshes. In the latter case, the fractal dimension of the porous structures obtained was calculated directly.

In heavily doped silicon ($p > 10^{17}$ cm^{-3}) the electric charge focusing the lines of the electric field is concentrated on irregularities of the anode surface. The current density **j** is distributed over the anode surface nonuniformly. The ionic charge is depleted, but it is concentrated predominantly at pore tips where **j** is higher than the volume average. Near the pore tips ions are attracted to asperities, where the hole density is elevated. According to Ref. 8, this mechanism promotes electropolishing. A characteristic feature of this model is that for each charge carrier near a pore tip the zone where a hole is attracted to an asperity on the surface of the silicon anode is limited by some distance R_A. As a result, etching can occur only at pore tips without the entire surface being electropolished. We assume that an energy barrier is present at the walls of pores in p^+-Si that prevents holes which appear at the pore walls as a result of thermal generation from penetrating into the pores, while it is overcome at the pore tips, where the lines of the electric field are focused.

The numerical simulation of the anodization of p^+-Si was performed on a two-dimensional mesh (160×160). Each position on the mesh is defined as a cell. A mesh step corresponds to the spatial extent of the fluctuation of the surface charge. N holes undergo random transport, hopping over a distance equal to the mean free path (Fig. 1). As soon as a hole is located within the distance $R = n_P^{-3}$ from the nearest pore tip (n_P is the impurity density), drift in the direction of this tip starts. After the hole reaches a point on the interface, the curvature of the boundary within an interval L on both sides of this

point is analyzed. Decomposition occurs on the sharpest asperities within this interval. The quantity L corresponds to R_A and depends on the HF concentration and current density as

$$L \approx A(\mathbf{j}/c)^{1/2}, \tag{1}$$

where L is the number of mesh cells, $\mathbf{j}$ and c are expressed in the units mA/cm^2 and wt.%, respectively, and $A = 48$ (cm^{2}wt.%/mA)$^{1/2}$.

In a lightly doped crystal ($p < 10^{16}$ cm^{-3}) the space-charge density and intensity of the electric fields are low. For this reason, in these crystals the dominant pore formation mechanisms are hole diffusion, thermal generation, and recombination and in nanocrystals the size-quantization effect is the dominant mechanism. As is well known, size quantization increases the band gap. As a result, an energy barrier preventing hole penetration into nanoparticles arises between the nanoparticles and the bulk material. Size quantization becomes important on scales of the order of 10 nm.

Computer simulation of pore formation in p^--Si is performed on two-dimensional meshes (160×160) and three-dimensional ($160 \times 160 \times 80$) meshes. One mesh step corresponds to the average interatomic distance. The algorithm differs from the one described above: Before undergoing a hop, a hole can vanish and appear at a different point in the crystal. The probability of such an event is $\sim \exp(-E_G/kT)$, where E_G is the band gap. When a hole reaches a point on the interface, the neighborhood of the crystal near this point is analyzed. If the crystal contains a sphere with radius R_Q, then decomposition occurs. Otherwise, the hole continues its random motion.

The three-dimensional structures obtained were analyzed numerically. The porosity was calculated as a function of depth:

$$P(h) = N_{PS}(h)/N_{ij}(h), \tag{2}$$

where $N_{PS}(h)$ is the number of cells contained in the pores in a layer of depth h and $N_{ij}(h)$ is the total number of cells in this layer.

The fractal dimension of the porous structures was calculated by the ''sandbox'' method[12] as

$$D(i,j,k) = 3\log_{ijk/i^*j^*k^*} \frac{N_{PD}(i,j,k)}{N_{PD}(i^*,j^*,k^*)}, \tag{3}$$

where $N_{PD}(x,\ y,\ z)$ is the number of crystal cells contained in a parallelepiped $x \times y \times z$ ($x \geqslant 1$, $y \geqslant 1$, $z \geqslant 1$) centered at some site of the crystal, averaged over all such sites. The neighboring quantities (i,j,k) and (i^*,j^*,k^*) differed by not more than 1.

An array of pictures obtained by numerical simulation on a (160×160) two-dimensional mesh for $N = 80$ is presented in Fig. 2. The black color represents pores. In each picture the pores grow from top to bottom. The rows and columns in the array are labeled with the values of the effective model parameters R and L. One can see that the pore diameter increases with L; this corresponds to increasing current density and/or decreasing HF concentration. Within the diameter, L pores are continuous in the lateral direction, in agreement with high-resolution transmission electron microscopy (TEM) results for micro- and macroporous layers of silicon.[13] Continuity is achieved by includ-

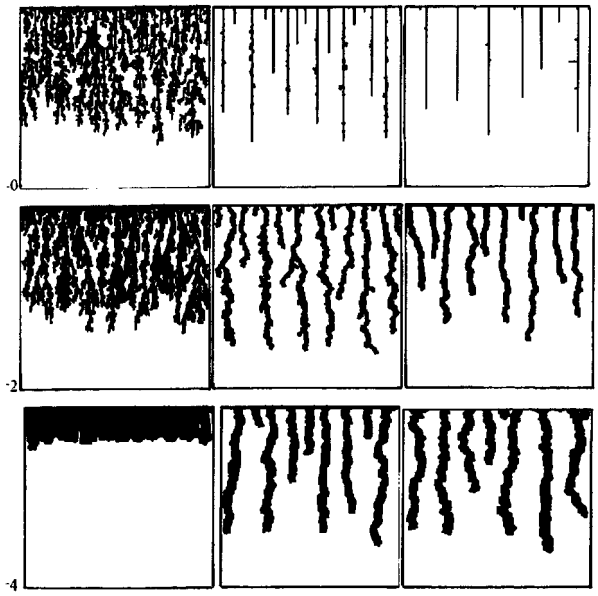

FIG. 2. Array of pictures of a porous structure which were obtained by varying the model parameters L and R ($N=80$). The pores are colored black and grow from top to bottom.

ing in the simulation a factor R_A, since simulation based on the standard diffusion-limited model makes it possible to obtain only branched pores.[6,10] For $L=4$ and $R=0$ the current density is high enough for electropolishing to occur. As R increases, the pores become longer and the interpore distance increases. For $L=0$ and $R=10$ and 20 the direction of growth is practically predetermined, since the active zone for each pore is limited by its lowest point. In Ref. 14 similar conditions were realized in *n*-Si by using small initial pits and back-side illumination. The structures obtained by simulation and experimentally were compared with the TEM data obtained for samples of porous silicon in the experiments of Refs. 13 and 15.

A matrix of sections of the obtained three-dimensional structures ($160\times160\times80$) along planes parallel to the surface of the substrate for $N=3000$, whose rows and columns correspond to the relative depth $h/h_{\max}$ and the generation probability G, was constructed. The parameter R_Q was set equal to 3 lattice sites. The calculations showed that the quantity dP/dh decreases when hole thermal generation and recombination factors are incorporated in the model. The curves $P(h/h_{\max})$, where $h_{\max}$ is the maximum depth of the pores, are displayed in Fig. 3. The steep slope near the initial boundary is due to the difference in the growth conditions of the pores on the initial surface and at some depth. The thickness of the transitional layer between the porous and continuous silicon decreases with increasing scale on which size quantization is manifested with a sufficiently large thermal generation factor ($G=0.5$). Our investigations also established that decreasing G increases the porosity gradient along the depth of the main layer of porous silicon.

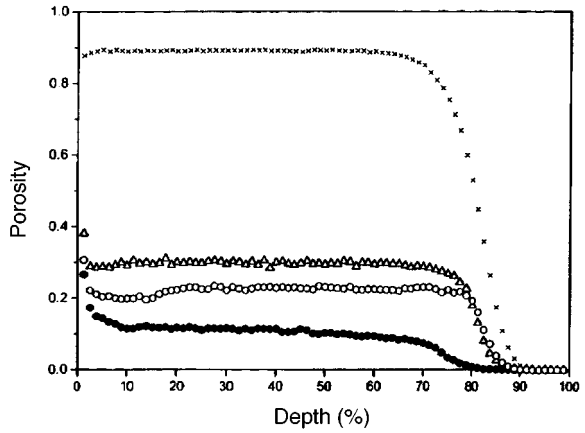

FIG. 3. Porosity versus depth for structures obtained by simulation on a three-dimensional mesh (× — $R_Q=1$, Δ — $R_Q=2$, ○ — $R_Q=3$, ● — $R_Q=4$; $G=0.05$).

The fractal dimension was calculated from Eq. (3) for crystalline structures obtained by numerical simulation on a three-dimensional mesh. The dependence of the fractal dimension on the size of the structure (defined as $\sqrt[3]{i \cdot j \cdot k}$) is shown in Fig. 4. It varies from 0.1 to 3 for structures ranging in size from 1.3 to 4 mesh cells, which corresponds to real values from 0.3 to 1 nm. To each abscissa $\sqrt[3]{i \cdot j \cdot k}$, whose value can be obtained with at least three combinations of i, j, and k, there correspond at least three points. Most points with the same abscissas are superposed on one another, showing that the fractal properties of the structures obtained are isotropic. Neutron-scattering experiments[16] showed that the mesoporous structures possess a fractal dimensionality on scales of up to

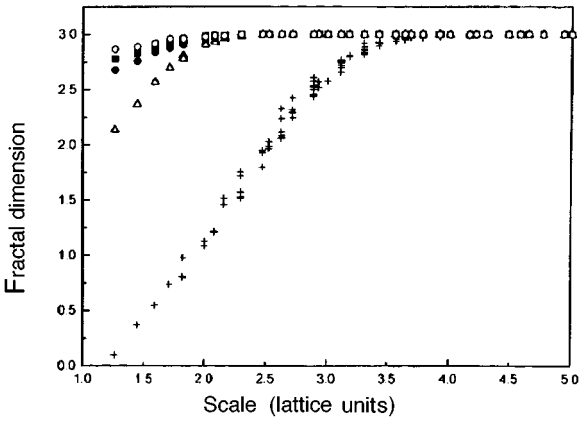

FIG. 4. Fractal dimension of structures obtained by simulation on a three-dimensional mesh as a function of the size: + — $R_Q=1$, $G=0.05$; △ — $R_Q=1$, $G=0.015$; ● — $R_Q=2$, $G=0.015$; ○ — $R_Q=3$, $G=0.05$; □ — $R_Q=4$, $G=0.05$.

100 nm. The fractal nature of the nanoporous silicon structures should be manifested on shorter scales.

The model presented above gives a more accurate description of the process leading to the formation of porous silicon. It includes a relief-dependent etching mechanism, which produces macropores of different diameters and shapes. In the case of p^--Si the model takes account of thermal generation and recombination of holes as well as the size quantization in nanocrystals. The transverse sections of the structures obtained by simulation and experimentally look similar. Analysis of the porous structures obtained by simulation on a three-dimensional mesh showed that the porosity and its depth gradient depend strongly on the size-quantization scale and the generation–recombination factor, respectively. The fractal dimension calculated directly for the simulated nanoporous structures assumes ranges from 0.1 to 3 on scales ranging from 0.3 to 1 nm.

[a)]e-mail: aleks@ns.isp.nsc.ru

[1]L. T. Canham, Appl. Phys. Lett. **57**, 1046 (1990).
[2]V. Lehmann, W. Honlein, H. Reisinger *et al.*, Thin Solid Films **276**, 138 (1996).
[3]S. Konaka, M. Tabe, and T. Sakai, Appl. Phys. Lett. **41**, 86 (1982).
[4]V. G. Shengurov, V. N. Shabanov, N. V. Gudkova, and B. Ya. Tkach, Mikroélektronika **222,** 19 (1993).
[5]L. N. Aleksandrov and P. L. Novikov, Phys. Status Solidi A **158** 419 (1996).
[6]R. L. Smith, S.-F. Chuang, and S. D. Collins, J. Electron. Mater. **17**, 533 (1988).
[7]L. N. Aleksandrov and P. N. Novikov, *Thin Films in Electronics* [in Russian], Tekhnomash, Moscow, 1996.
[8]V. Lehmann, Thin Solid Films **255**, 1 (1995).
[9]V. Lehmann and U. Gösele, Appl. Phys. Lett. **58**, 856 (1991).
[10]M. I. J. Beale, N. G. Chew, M. J. Uren *et al.*, Appl. Phys. Lett. **46**, 86 (1985).
[11]Z. J. He, Y. P. Huang, and R. Kwor, Thin Solid Films **265**, 96 (1995).
[12]L. Forrest and T. A. Witten, J. Phys. A **12**, L109 (1979).
[13]C. H. Lee, C. C. Yeh, H. L. Hwang, and Klaus Y. J. Hsu, Thin Solid Films **276**, 147 (1996).
[14]V. Lehmann, F. Hofmann, F. Müller, and U. Crüming, Thin Solid Films **255**, 20 (1995).
[15]E. zur Mühlen, Da Chang, S. Rogashevski, and H. Niehus, Phys. Status Solidi B **198**, 673 (1996).
[16]B. J. Heuser, S. Spooner, G. J. Glinka *et al.*, Mater. Res. Soc. Symp. Proc. **283**, 209 (1993).

Translated by M. E. Alferieff

Investigation of level crossing in the tetragonal paramagnet $YbPO_4$ in ultrahigh magnetic fields up to 400 T

Z. A. Kazeĭ[a)] and R. Z. Levitin
Department of Physics, Moscow State University, 119899 Moscow, Russia

N. P. Kolmakova and A. A. Sidorenko
Technical University, 241035 Bryansk, Russia

V. V. Platonov and O. M. Tatsenko
Russian Federal Nuclear Center, 607190 Sarov, Nizhegorod Region, Russia

(Submitted 7 April 1997)
Pis'ma Zh. Éksp. Teor. Fiz. **65**, No. 9, 691–694 (10 May 1997)

The crossing of the energy levels of Yb^{3+} ions in paramagnetic $YbPO_4$ in ultrahigh magnetic fields of up to 400 T, produced by an explosive method, is investigated experimentally and theoretically. A wide maximum is found in the differential susceptibility dM/dH in a field $H_c \approx 280$ T. This maximum is due to the crossing of the energy levels of the magnetic ions in the field. The magnetocalorimetric effect is calculated under the assumption that the magnetization process in the pulsed fields is adiabatic. The effect is nonmonotonic as a function of the field and is accompanied by a substantial cooling of the crystal near H_c. © *1997 American Institute of Physics.*
[S0021-3640(97)00409-X]

PACS numbers: 75.20.−g, 33.80.Be

Crossing of the energy levels of magnetic ions in a field (crossover) and an associated jump in magnetization have been predicted theoretically[1] for the compound TmSb and have been observed experimentally in various rare-earth (RE) compounds (see, for example, Ref. 2) in both paramagnetic and ordered states. This effect occurs when the energy of the lower level of the crystal-field-split ground-state multiplet of the RE ion depends on the magnetic field much more weakly than the energy of one of the excited multiplets. For this reason, in sufficiently high fields these levels first draw together and then exchange places. Since in this case the more ''magnetic'' level becomes the ground-state level, crossover is accompanied by an abrupt increase in the magnetization M and a maximum in the differential susceptibility dM/dH.

It can be expected that level crossing effects will be quite numerous in the RE zircons RXO_4 (R is a rare-earth ion, X = As, P, V), since the quite low tetragonal symmetry of zircon (space group $D_{4h}^{19} = I4_1/amd$) gives a rich, weakly degenerate, spectrum of the RE ion and an appreciable magnetic anisotropy in directions parallel to and perpendicular to the tetragonal axis in the paramagnetic state. Since there are no nonequivalent positions for a RE ion in the zircon structure, these effects should be clearly

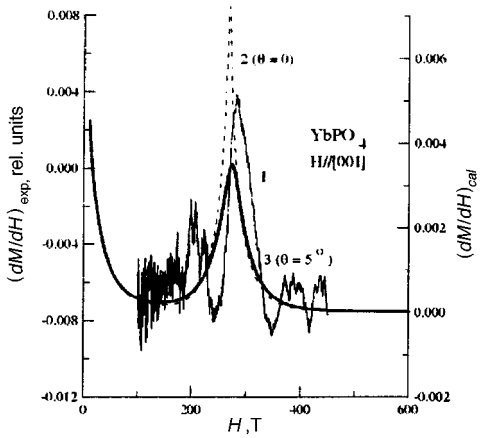

FIG. 1. Experimental (*1*) and computed (*2, 3*) dependences of the differential susceptibility dM/dH for $YbPO_4$ for magnetic field orientation near the tetragonal axis [001] (θ — angle of orientation).

observed even in macroscopic characteristics such as the magnetization. Of the entire series of RE zircons, crossover in comparatively weak magnetic fields ($\sim$10 T) has been investigated thus far only in paramagnetic $HoVO_4$.[3–5] The substantial progress made in producing high and ultrahigh magnetic fields makes level crossing effects now accessible for experimental investigation. In the present work we investigated level crossing in paramagnetic $YbPO_4$ both experimentally and theoretically.

The measurements were performed on a $YbPO_4$ single crystal at 4.2 K by an induction method in pulsed magnetic fields of up to 400 T, produced by an explosive method.[6] The rise time of the field in the pulse was equal to 15 μs. These are one-time measurements and the measuring coils and samples are destroyed after each pulse; it is impossible to compensate the signal from the magnetic field completely. Therefore the signal induced in the measuring coils can be written in the form

$$V_1(H) \sim \frac{dM}{dt} + K\frac{dH}{dt}, \tag{1}$$

where the first term corresponds to the signal from the sample and the second term corresponds to the coil decompensation signal. During the field pulse the signals V_1 and $V_2 \sim dH/dt$ from the measuring and ''field'' coils were recorded every 0.002 μs (approximately 8000 points). These data make it possible to calculate the curves $V_1(H)/V_2(H)$ (which, assuming that the decompensation signal is only a weak function of the field intensity, are proportional with proportionality constant K to the differential susceptibility of the sample $dM/dH=(dM/dt)/(dH/dt)$ and also to time-average the signal in order to decrease the high-frequency fluctuations of the background.

Figure 1 displays the experimental and theoretical curves of dM/dH for a $YbPO_4$ single crystal for a magnetic field oriented along the tetragonal axis [001]. The wide maximum of the susceptibility at $H_c \approx 280$ T is due to the crossing of the energy levels of the Yb^{3+} ion. The large width of the maximum is apparently due to the change in the

temperature of the sample as a result of the magnetocaloric effect accompanying magnetization in a pulsed field. Since the spin–lattice relaxation time in RE ionic compounds is very short ($\sim 10^{-9}$ s; see, for example, Ref. 7) compared with the duration of the field pulse, the electronic subsystem and lattice are in equilibrium during the measurements and the magnetization process is close to adiabatic. In our view, the heat transfer between the sample and the surrounding medium is very weak, even in pulsed fields with duration ~ 10 ms, as is indicated by the fact that the magnetization curves with increasing and decreasing field are the same.

The Zeeman effect and the magnetic characteristics were calculated using a Hamiltonian that includes the crystal-field Hamiltonian, written in terms of the irreducible tensor operators C_q^k, and a Zeeman term:

$$H = B_0^2 C_0^2 + B_0^4 C_0^4 + B_0^6 C_0^6 + B_4^4 (C_4^4 + C_{-4}^4) + B_4^6 (C_4^6 + C_{-4}^6) + g_J \mu_B \mathbf{H} \cdot \mathbf{J}. \quad (2)$$

Here B_q^k are the crystal-field parameters and g_J is the Landé factor. The crystal-field parameters for the Yb^{3+} ion in the phosphate matrix are known only for the doped compounds Yb:$LuPO_4$ and Yb:YPO_4 (Ref. 8) (the parameters B_0^2 of these compounds are substantially different) and can, generally speaking, differ appreciably from the values for the concentrated $YbPO_4$ compound. The crossover field H_c is determined by the spectrum and wave functions of the ground-state multiplet $2F_{7/2}$ of the Yb^{3+} ion, which are formed by the crystal field. Our calculations of H_c with the crystal-field parameters for Yb:YPO_4 and Yb:$LiPO_4$ give values of 210 T and 180 T, respectively. Numerical analysis shows that the value of the crossover field is most sensitive to the parameter B_0^2. Solving the optimization problem for $YbPO_4$ taking account of all available information (from spectroscopy and ESR[8,9] as well as our magnetic measurements) gives crystal-field parameters which fall within their range of variation in the series of RE phosphates and yields the theoretical value $H_c = 270$ T. This value agrees well with the experimental value within the error limits associated with measurement of the field ($\pm 10\%$) and a possible disorientation of the sample of $\leqslant 3°$.

An interesting feature of crossover in $YbPO_4$ is that the ground-state level ($g_z^{\mathrm{gr}} \sim 2$) crosses the bottom level of the first excited doublet, for which the z-component of the g-tensor in the absence of a magnetic field is much smaller ($g_z^{\mathrm{ex1}} < 0.1$). In a field, however, the third excited doublet is strongly admixed to the bottom level of the first excited doublet of the state $|+7/2\rangle$, both states belonging to the same representation, and a large increase occurs in the g_z factor of the latter. For the ground-state doublet g_z does not change as strongly in a field because of the weak admixture of the second excited doublet to it. We note that for a field orientation strictly in the direction of the tetragonal axis there is no mixing of the wave functions of the ground-state and first excited doublets and for this reason the ''true'' level crossing should be observed. A misorientation of the field by even 3–5° causes components $|\pm 7/2\rangle$ to appear in the wave function of the ground state and in the interaction between the ground-state and first excited levels, which gives rise to a small gap (level repulsion) in the spectrum near the crossover fields. This results in broadening of the maximum in dM/dH and increases the crossover field.

In calculating the magnetic characteristics for fields from 0 to 400 T with step $\Delta H = 0.01$ T, the Hamiltonian (2) was diagonalized numerically in order to determine the

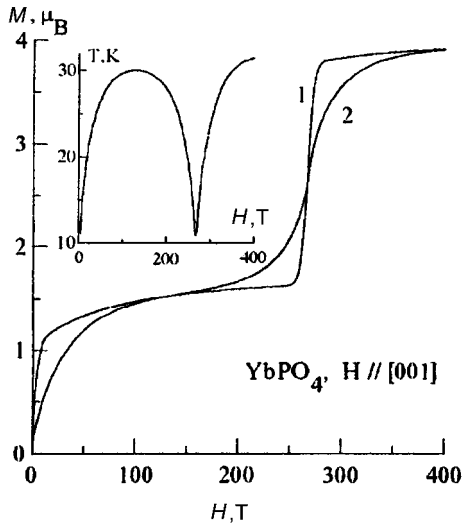

FIG. 2. Isothermal (*1*) and adiabatic (*2*) magnetization curves $M(H)$ for $YbPO_4$ for the initial temperature $T_0=4.2$ K and variation of the temperature $T(H)$ of the sample due to the magnetocaloric effect accompanying adiabatic magnetization.

spectrum and the wave functions of the Yb^{3+} ion, and the ''elementary'' magnetocaloric effect ΔT accompanying a change in the field from H to $H+\Delta H$ was calculated:

$$\Delta T=-(\partial M/\partial T)_H T\Delta H/C_H. \tag{3}$$

In this formula the total specific heat C_H of the crystal includes the lattice specific heat $C_{\text{lat}}\sim(T/T_D)^3$ (the Debye temperature for the phosphate lattice $T_D=275$ K[10]) and the magnetic specific heat C_{mag}, calculated for each value of the field and temperature on the basis of the spectrum of the RE ion. These data made it possible to calculate the isothermal and adiabatic magnetization of $YbPO_4$ and the temperature of the sample as a function of the magnetic field (Fig. 2). The latter function is nonmonotonic, i.e., at first the sample is heated by approximately 25 K and then it cools down by approximately 20 K in the region of the crossover fields. The sign of the ''elementary'' magnetocaloric effect is determined by the sign of the derivative $(\partial M/\partial T)_H$. For isothermal magnetization curves with jumps this derivative is positive as the crossover field is approached (heating smooths the jumps), which explains the cooling of the crystal near crossover.

Level-crossing investigations yield a great deal of information about the spectrum and wave functions of the RE ion, and ultimately their purpose is to investigate the crystal field. The good agreement between the computed and experimental data for $YbPO_4$ confirms that the magnetization process in an ultrahigh field is nearly adiabatic. Depending on the character of the levels participating in crossover, both heating and cooling of the sample can be observed near crossover. Cooling of the crystal gives anomalies of the magnetic characteristics that in a number of cases are even more pronounced than for an isothermal process in static fields. This makes it possible to investigate crossover effects by performing magnetic measurements in high and ultrahigh

pulsed fields. We underscore that, as our calculations show, such effects can be expected for an entire series of compounds from the group of RE oxides with the zircon structure.

[a)]e-mail: kazei@plm2phys.msu.su

---

[1] B. R. Cooper, Phys. Lett. **22**, 244 (1966).
[2] M. Guillot, A. Marchand, V. Nekvasil, and F. Tcheou, J. Phys. C **18**, 3547 (1985).
[3] J. E. Battison, A. Kasten, M. J. M. Leask, and J. B. Lowry, J. Phys. C **10**, 323 (1977).
[4] T. Goto, A. Tamaki, T. Fujimura, and H. Unoki, J. Phys. Soc. Jpn. **55**, 1613 (1986).
[5] P. Morin, J. Rouchy, and Z. Kazei, Phys. Rev. B **51**, 15103 (1995).
[6] A. I. Pavlovskii, N. P. Kolokol'chikov, and O. M. Tatsenko, *Megagauss Physics and Techniques*, edited by P. Turchi, Plenum Press, New York, 1980.
[7] Landolt-Bornstein, *Numerical Data and Functional Relationships in Science and Technology*, vol.27/e, edited by H. P. J. Wijn, Springer-Verlag, Berlin, 1991.
[8] P. C. Becker, T. Hayhurst, G. Shalimoff *et al.*, J. Chem. Phys. **81**, 2872 (1984).
[9] P. C. Becker, N. Edelstain, G. M. Willians *et al.*, Phys. Rev. B **45**, 5027 (1992).
[10] A. Kasten, H. G. Kahle, P. Klofer, and D. Schafer-Siebert, Phys. Status Solidi B **144**, 423 (1987).

Translated by M. E. Alferieff

Nematic LC to nematic glass phase transition in pores

E. I. Kats
L. D. Landau Institute of Theoretical Physics, Russian Academy of Sciences, 117940 Moscow, Russia

(Submitted 7 April 1997)
Pis'ma Zh. Éksp. Teor. Fiz. **65**, No. 9, 695–698 (10 May 1997)

The properties of a nematic liquid crystal in a porous matrix are discussed. On scales exceeding a certain characteristic scale the liquid crystal behaves as a nematic glass. Application of a weak magnetic field restores long-range orientational order. © *1997 American Institute of Physics.* [S0021-3640(97)00509-4]

PACS numbers: 64.70.Md

1. Porous media (specifically, so-called aerogels) are convenient systems for studying the role of surface interactions and the physical properties of different systems. In the early stages of this research it was mainly the character of the filling of the pores with simple liquids and the very structure of the porous media that were studied, but in the last few years more subtle effects pertaining to the behavior of superfluid helium[1] or liquid crystals have gained priority (see, for example, Refs. 2–5 and the literature cited therein).

Roughly speaking, there are two types of effects for a nematic liquid crystal confined in a porous matrix. First, there is a direct interaction with the pore surface and, second, there is a simple restriction of the volume accessible to the liquid crystal. The interaction with the surface itself also has a dual effect on the liquid crystal. On the one hand, it influences the modulus of the order parameter (in this way it suppresses or stimulates the phase transition from the nematic LC to the isotropic liquid) and, on the other, it has an orienting effect on the director **n** of the liquid crystal (this part of the surface energy is traditionally called the anchoring energy).

The direct interaction with the surface can result in a shift of the transition temperature. The first-order nematic–isotropic liquid phase transition occurs when the thermodynamic potentials Ω of the two phases and also their chemical potentials are equal:

$$\Omega_I(T_c+\Delta T)+\frac{c\gamma_I}{R}=\Omega_N(T_c+\Delta T)+\frac{c\gamma_N}{R}. \tag{1}$$

Here R is the characteristic pore radius (it is assumed that the pore-size distribution is quite narrow), T_c is the temperature of the nematic–isotropic liquid transition in the bulk, γ is the surface tension, c is a numerical factor that depends only on the pore geometry, and the indices I and N designate isotropic and nematic phases, respectively. From the relation (1) we find for the shift of the transition temperature

$$\Delta T=\frac{cT_c(\gamma_N-\gamma_I)}{QR}, \tag{2}$$

where Q is the latent heat of the transition.

As a result of the limitation on the volume accessible for the liquid crystal, first, the phase transition itself becomes diffuse (since the increase in the correlation length stops at the pore size) and, second, the transition temperature decreases as $\propto 1/R^2$ (in contrast to the effect studied above which $\propto 1/R$ and whose sign is not fixed from general considerations).

However, the effects described above are related with the individual action of the pore surface and in no way take account of the interpore coupling. In contrast to this, the coupling interaction between the orientation and the aerogel surface is of a collective character and therefore influences not only the behavior of the liquid crystal in an individual pore but also the entire macroscopic system. This letter is devoted to an analysis of this effect.

2. The free energy of a nematic liquid crystal filling a porous matrix can be represented as a sum of the following contributions

$$F = F_g + F_a + F_m . \tag{3}$$

Here F_g is the Frank (gradient) energy, F_a is the anchoring energyorientation–surface of the orientation with the surface, and F_m is the interaction energy of the liquid crystal with the external magnetic field. The expressions for these contributions are all well known.[6] The Frank energy in a one-constant approximation has the form

$$F_g = \frac{1}{2} K \int dV (\nabla \cdot \mathbf{n})^2, \tag{4}$$

where K is the Frank elastic elastic ($\sim 10^{-6}$ erg/cm) and $\mathbf{n}$ is the unit vector of the director.

The anchoring energy is

$$F_a = \frac{1}{2} W \int dS (\mathbf{n} \cdot \mathbf{l})^2, \tag{5}$$

where W is the characteristic anchoring energy of the orientation with the surface, and $\mathbf{l}$ is a unit vector normal to the surface. The value of W varies over quite wide limits depending on the material and the physicochemical treatment of the surface ($W \sim 10^{-2} - 1$ erg/cm^2). The integral in Eq. (5) extends over the surface of the porous matrix and therefore it is proportional to the density of the aerogel.

Finally,

$$F_m = -\frac{1}{2} \chi_a \int dV (\mathbf{H} \cdot \mathbf{n})^2, \tag{6}$$

where χ_a is the anisotropy of the diamagnetic susceptibility of the liquid crystal ($\sim 10^{-7}$) and $\mathbf{H}$ is the external magnetic field.

The contributions to the energy (4)–(6) entering in F determine several characteristic length scales. First, there is the penetration depth of the surface disturbances into the volume:

$$\lambda_s = \frac{K}{W}. \tag{7}$$

Second, there is the magnetic coherence length

$$\xi_H = \frac{W}{\chi_a H^2}. \tag{8}$$

Third, there exists, of course, a characteristic geometric size — the pore radius R. Finally, the correlation length ξ plays a large role near a phase transition (and for liquid crystals this is virtually the entire region of existence of the nematic LC).

Let $\xi \gg R$ (for aerogels this holds in the entire region of existence of the nematic phase, since in typical cases $R \sim 20$–30 Å, while $\xi \sim 10^2$–10^3 Å). For this reason, the surface energy (5) formally plays the role of anisotropic and randomly oriented impurities. As is well known,[7] a random local anisotropy leads in three-dimensional systems to breakdown of orientational order on large scales. The characteristic scale Λ on which this breakdown occurs can be found as follows. On this scale the gain in energy due to the random surface coupling is compensated by the elastic energy loss. Therefore, comparing Eqs. (4) and (5), we obtain

$$WR^2 c^{1/2} \simeq K\Lambda, \tag{9}$$

where c is the concentration of the random ''impurities'' on the scale Λ:

$$c \simeq \frac{\Lambda^3}{R^3}. \tag{10}$$

From Eqs. (9) and (10), taking account of the definition (7), we find

$$\Lambda = \frac{\lambda_s^2}{R}. \tag{11}$$

Orientational order breaks down on scales of the order of Λ and larger. Over large distances Λ the nematic liquid crystal in the porous aerogel matrix behaves as an anisotropic glass, i.e., $\langle \mathbf{n}(\mathbf{r}) \rangle = 0$, but the stiffness with respect to nonuniform deformations of $\mathbf{n}$ remains. More accurately, this fact means that in this state of a nematic glass the standard nematic order parameter (symmetric traceless tensor of rank 2) equals zero:

$$\langle Q_{\alpha\beta}(\mathbf{r}) \rangle = 0.$$

However, the bilinear averages are different from zero, and they play the role of the order parameter of the nematic glass

$$\langle Q_{\alpha\beta} Q_{\gamma\delta} \rangle = S_{\alpha\beta\gamma\delta}(\mathbf{r}).$$

At the same time, the application of a sufficiently strong external magnetic field restores the long-range orientational order. The critical field H_c is determined from the condition that the magnetic energy F_m is greater than the random-anisotropy energy

$$WR^2 \left(\frac{\Lambda}{R} \right)^{3/2} = \chi_a H_c^2 \Lambda^3. \tag{12}$$

Using the definitions (7) and (11), we find

$$H_c = \frac{1}{\sqrt{\chi_a}} \frac{W}{R} \left(\frac{R}{\lambda_s} \right)^3 . \tag{13}$$

Therefore a nematic LC to nematic glass phase transition occurs in the field H_c.

I thank G. E. Volovik for stimulating the writing of this letter and for acquainting me with helpful literature on this question. This work was supported under the state program ''Statistical Physics'' of the Ministry of Science and in part under INTAS Grant No. 94-40-78 and by the Russian Fund for Fundamental Research.

[1] G. E. Volovik, JETP Lett. **63**, 301 (1996).
[2] N. Clark, T. Bellini, R. M. Malzender *et al.*, Phys. Rev. Lett. **71**, 3505 (1993).
[3] S. Tripathe, Ch. Rosenblatt, and F. M. Aliev, Phys. Rev. Lett. **72**, 2725 (1994).
[4] T. Bellini, A. G. Rappaport, N. A. Clark, and B. N. Thomas, Phys. Rev. Lett. **77**, 2507 (1996).
[5] L. Radzihovsky and J. Toner, LANL e-print archive, cond-mat/9702011.
[6] P. G. de Gennes, *The Physics of Liquid Crystals*, Clarendon Press, Oxford, 1974 [Russian translation, Mir, Moscow, 1977].
[7] Y. Imri and S. Ma, Phys. Rev. Lett. **35**, 1399 (1975).

Translated by M. E. Alferieff

Electronic structure of ultrathin Cs coatings on a Si(100) 2×1 surface

G. V. Benemanskaya and D. V. Daĭneka
A. F. Ioffe Physicotechnical Institute, Russian Academy of Sciences, 194021 St. Petersburg, Russia

F. É. Frank-Kamenetskaya
St. Petersburg Technological Institute, 198013 St. Petersburg, Russia

(Submitted 11 April 1997)
Pis'ma Zh. Éksp. Teor. Fiz. **65**, No. 9, 699–702 (10 May 1997)

The electronic structure and ionization energy of submonolayer Cs coatings on a Si(100)2×1 surface is investigated by threshold photoemission spectroscopy. Two surface bands induced by Cs adsorption are observed, and their evolution is studied as a function of coverage. It is found that there are two ''adsorption locations'' for Cs atoms, where they interact with active dangling bonds at the surface. It has been determined that the Cs/Si(100)2×1 interface is semiconducting all the way down to monolayer coverage. The results show that Cs adsorption is predominantly of a covalent character. © *1997 American Institute of Physics.* [S0021-3640(97)00609-9]

PACS numbers: 73.61.At, 79.60.Bm, 79.60.Dp, 42.79.Wc

The increased attention directed toward investigations of adsorption properties and local interactions on different reconstructed silicon surfaces coated with alkali metal atoms is due to the promising applications of such systems in nanotechnology for the production of regular structures of small dimensions. As investigations performed in the last few years have shown, the dimer-reconstructed surface Si(100)2×1 possesses semiconductor-like electronic surface structure.[1,2] It is thought that a Si(100)2×1 surface has two dangling bonds per dimer, i.e., the density of dangling bonds equals the density of surface atoms $n=6.7\cdot10^{14}$ cm^{-2} (1 ML). We note that 1 ML is defined as the density of atoms of the unreconstructed Si(100)1×1 surface. On adsorption of Cs the dimer structure of the surface remains and the adatoms can occupy different positions, so-called ''adsorption locations,'' above the dimers, between atoms in a dimer, between dimers, and so on, which should affect the energy characteristics of the interfaces. The theoretical calculations are based on two alternative models of the adsorption process — the Levine model[3,4] and the double-layer model.[5,6] In these models both the number of adsorption locations and the saturating coverage are important factors. However, the number of locations has not been determined experimentally for the Cs/Si(100)2×1 system. The value of the saturating Cs coverage is also uncertain, taken as 0.5 ML according to one set of data[7] and close to 1 ML according to another set.[8] In contrast to detailed photoemission investigations of the electronic surface structure for K/Si(100)2×1 and Na/Si(100)2×1 interfaces, similar investigations have not been performed for Cs/Si(100)2×1.

We investigated the surface photoemission and determined the ionization energy for the system Cs/Si(100)2×1. Two bands induced by Cs adsorption were observed in the spectrum at submonolayer coverages. This shows that the local interactions of the $6s$ valence states of the Cs atoms and the $s-p^3$ orbital of the dangling bonds of the surface are different at different adsorption locations. It was determined that the development of the Cs bands is completed at a coverage corresponding to the minimum ionization energy and close to 1 ML. It was established that at coverages all the way up to 1 ML an energy gap exists in the spectrum of the surface states and the Cs/Si(100)2×1 interface exhibits a semiconductor character.

The measurements were performed *in situ* under ultrahigh-vacuum conditions $P<2\cdot10^{-10}$ torr at room temperature. A pure Si(100)2×1 surface (p-type, 7.5 $\Omega\cdot$cm) was obtained after a thin oxide layer was removed and standard multistep annealing was performed.[9] The method of threshold photoemission spectroscopy with excitation by s- and p-polarized light was used.[10] The method is based on separation of the volume and surface photoemissions as well as on the intensification of the local electromagnetic field at the surface. In the case of s-polarization, only volume states of the substrate are excited with a threshold $h\nu_s$, which corresponds to the position of the valence band top (VBT) in the bulk, i.e., the ionization energy ϕ. In the case of p-polarization surface electronic bands can be excited with threshold $h\nu_p$ as a result of the interaction with the normal component of the electric vector of the light. If the surface band is located at the Fermi level E_F (metallization case) or possesses an edge between the VBT and E_F, then the thresholds can differ substantially, $h\nu_s\neq h\nu_p$. In this case, the threshold $h\nu_p$ is determined either by the position of E_F or by the position of the edge of the surface band. Analysis of surface photoemission spectra makes it possible to determine the energy position of the surface bands with resolution ~0.02 eV as well as to establish the presence or absence of a finite density of surface states at E_F.[11]

Adsorption of Cs on a Si(100)2×1 surface results in a sharp reduction of the photoemission thresholds. The change in the thresholds $h\nu_s=\phi$ and $h\nu_p$ as the Cs coverage increases from 0.4 to 1.3 ML is displayed in Fig. 1. The observed difference of the thresholds clearly indicates the existence of a surface band above the VBT. The difference between the thresholds decreases from 0.15 eV at a 0.4 ML coverage to 0.05 eV at 1 ML; this indicates that the edge of the surface band shifts in the direction of the VBT. Analysis of surface photoemission near threshold shows that the density of surface states at E_F equals 0, i.e., the edge of the surface band lies between the VBT and E_F. Thus it has been established that an energy gap is present in the spectrum of the surface states of the system Cs/Si(100)2×1 and there is no metallization of the interface at Cs coverages up to ~1.3 ML.

One can see from Fig. 1 that both thresholds have a weak minimum at the same coverage, which was determined to be 1 ML. The determination of the coverage for a submonolayer metallic coating on a semiconductor surface is a difficult and rarely solvable problem. Here we propose a new method for estimating the coating *in situ* according to the ratio of the Cs deposition times on the experimental Si(100)2×1 surface and on a clean W(110) surface, playing the role of a standard. Both samples were simultaneously present in the vacuum chamber and a manipulator was used to place the samples into the beam of Cs atoms. Crossed laser beams were used to check the accuracy of the placement

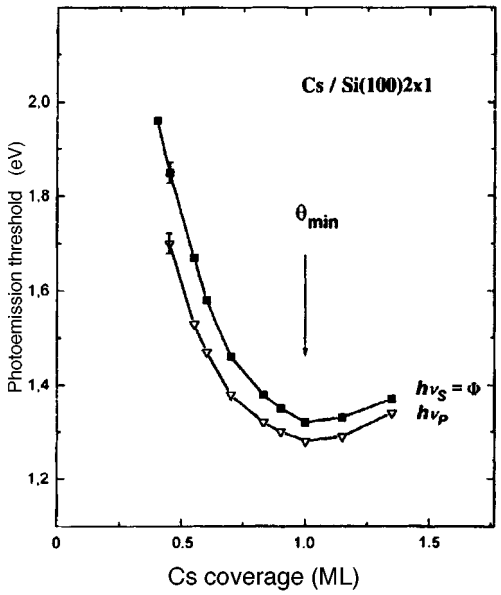

FIG. 1. Variation of the photoemission thresholds $h\nu_s$ and $h\nu_p$ for s- and p-polarized light, respectively, as a function of the Cs coverage on a Si(100)2×1 surface.

of the samples in the same position relative to the Cs source. Calibration was performed repeatedly. Figure 2 displays the concentration (Cs deposition time t) dependences of the photoemission current $I_s(t)$ with a constant energy of excitation by s-polarized light. This dependence has been well studied in the W(110) case, and it is known that the maximum corresponds to the minimum of the work function of the Cs/W(110) system

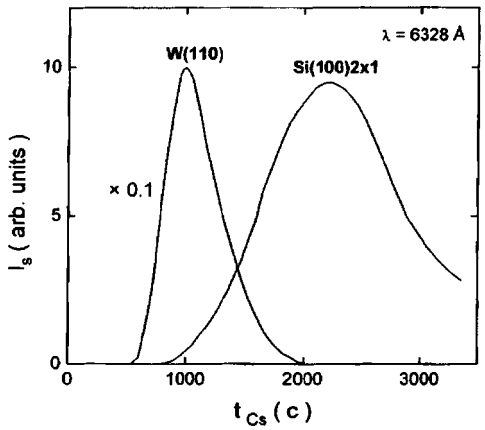

FIG. 2. Variation of the photoemission current I_s in the case of excitation with s-polarized light $\lambda = 6328$ Å as a function of the deposition time t of Cs atoms on a standard W(110) surface and on a Si(100)2×1 surface.

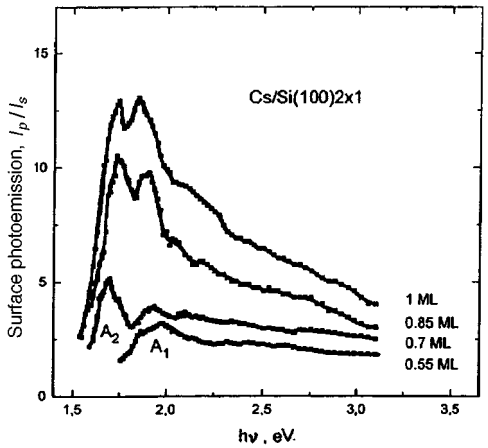

FIG. 3. Surface photoemission spectra I_p/I_s for a Cs/Si(100)2×1 system at different submonolayer Cs coverages.

with Cs adatom concentration on the surface $n\sim3.2\cdot10^{14}$ cm^{-2} (Ref. 12). In the Si(100) 2×1 case the dependence $I_s(t)$ reflects the variation of the ionization energy ϕ, so that the maximum of the curve corresponds to the minimum of ϕ. Therefore, the surface concentration of Cs adatoms on Cs/Si(100)2×1 can be estimated from the ratio of the deposition times at the minimum of ϕ as $\sim6.8\sim10^{14}$ cm^{-2}. It is important to note that the attachment coefficient in the case of Cs adsorption on the experimental and the standard surfaces equals 1 within a monolayer.

Figure 3 displays the surface photoemission spectra of the system Cs/Si(100)2×1 for different Cs coverages. The spectra reflect the local density of surface states below the VBT. A pronounced increase in the density of states and the formation of bands induced by Cs adsorption were found. It is also important to note that the form of the spectrum and the position of the bands indicate the existence of an energy gap in the spectrum of the surface states. In the case of a ~0.5 ML coverage a band A_1 with energy ~0.3 eV below the VBT appears in the spectrum. As the Cs coverage increases, the intensity of the band and its binding energy increase. At 1 ML the A_1 band lies 0.55 eV below the VBT. The A_2 band is observed in the spectrum at coverages greater than 0.65 ML. A similar increase of the binding energy with increasing coverage is observed, and at 1 ML the A_2 band lies 0.45 eV below the VBT.

Therefore adsorption of Cs on a Si(100)2×1 surface is predominantly of a covalent character and leads to the appearance of two bands below the VBT. The interface has semiconductor-type electronic structure, and metallization can be expected only with the formation of a second Cs layer. The development of the bands is completed at a coverage which corresponds to a minimum of ϕ and which was determined to be one monolayer. Therefore all dangling surface bonds participate in the adsorption process and the saturating coverage equals 1 ML.

Our experimental results all confirm the double-layer model.[5,6] In this model the Cs atoms occupy adsorption locations both above dimers — one type of local interactions —

and between dimers — another type of local interactions. As a result of the different character of the local interactions, the binding energies of the Cs adatoms are different and two induced bands A_1 and A_2 appear. The interface is of a semiconductor character in agreement with the theoretical calculations.[6]

This work was supported under Grant No. 96-2.28 of the program ''Surface atomic structures'' of the Ministry of Science of the Russian Federation.

[1] F. J. Himpsel and D. E. Eastman, J. Vac. Sci. Technol. **16**, 1297 (1979).
[2] J. Pollmann, P. Kruger, and A. Mazur, J. Vac. Sci. Technol. B **5**, 945 (1987).
[3] J. D. Levine, Surf. Sci. **34**, 90 (1973).
[4] M. Tsukada, H. Ishida, and N. Shima, Phys. Rev. Lett. **53**, 376 (1984).
[5] T. Abukawa and S. Kono, Phys. Rev. B **37**, 9097 (1988).
[6] I. P. Batra, Phys. Rev. B **39**, 3919 (1989).
[7] P. S. Mangat and P. Soukiassian, Phys. Rev. B **52**, 12020 (1995).
[8] A. J. Smith, W. R. Graham, and E. W. Plummer, Surf. Sci. **243**, L37 (1991); T. Urano, S. Hondo, and T. Kanaju, Surf. Sci. **287/288**, 294 (1993).
[9] F. Ishizaka and Y. Shiraki, J. Electrochem. Soc. **133**, 666 (1986).
[10] G. V. Benemanskaya, M. N. Lapushkin, and M. I. Urbakh, Zh. Éksp. Teor. Fiz. **102,** 1664 (1992) [Sov. Phys. JETP **75**, 899 (1992)].
[11] G. V. Benemanskaya, G. E. Frank-Kamenetskaya, and M. N. Lapushkin, Surf. Sci. **331–333**, 552 (1995).
[12] A. G. Fedorus and A. G. Naumovets, Surf. Sci. **21**, 426 (1975).

Translated by M. E. Alferieff

Observation of standing x-rays in Bragg diffraction on high-T_c superconducting crystals $Nd_{1.85}Ce_{0.15}CuO_{4-\delta}$

M. V. Koval'chuk and A. Ya. Kreĭnes
A. V. Shubnikov Institute of Crystallography, Russian Academy of Sciences, 117333 Moscow, Russia

Yu. A. Osip'yan
Institute of Solid-State Physics, Russian Academy of Sciences, 142432 Chernogolovka, Moscow Region, Russia

V. V. Kvardakov and V. A. Somenkov
Kurchatov Institute Russian Science Center, 123182 Moscow, Russia

(Submitted 11 April 1997)
Pis'ma Zh. Éksp. Teor. Fiz. **65**, No. 9, 703–706 (10 May 1997)

Curves of the secondary-fluorescence yield from the constituent elements of high-T_c superconducting crystals $Nd_{1.85}Ce_{0.15}CuO_{4-\delta}$ are measured in the dynamic x-ray diffraction regime. The form of the curves attests to the appearance of a standing x-ray wave in the crystal.
 [S0021-3640(97)00709-3]

PACS numbers: 61.10.Nz, 74.72.Jt

The study of the fine details of the structure of high-T_c superconductors is a very interesting physical problem. Specifically, an important problem is the characterization of the sublattices of atoms of a definite kind both to reveal defects in the corresponding atomic sublattice and from the standpoint of analyzing the preferred positions of different kinds of atoms in solid solutions of substitution. The method of standing x-ray waves,[1,2] which makes it possible to determine the position (coordinates) of different kinds of atoms in a lattice, can furnish answers to these questions. The method of standing x-ray waves is based on the use of a spatially modulated electromagnetic field, arising in a crystal during dynamic diffraction, to excite secondary radiation (specifically, fluorescence x-rays or photoelectrons) of the atoms in the crystal. By analyzing the angular dependence of the characteristic secondary radiation within the region of dynamic diffraction, the positions of the corresponding atoms relative to the system of diffraction planes can be determined to a high degree of accuracy and the degree of disorder of the atomic subsystem can be characterized. The possibilities of the method of standing x-ray waves, combining the structural (diffraction) resolution with spectroscopic sensitivity, were demonstrated in Refs. 3–5 for the example of the analysis of the structure of multicomponent crystals. It should be noted that the practical implementation of the method of standing x-ray waves involves substantial experimental difficulties, since precise angular positioning of the crystal must be combined with spectroscopically sensitive detection of the secondary radiation (i.e., here high-resolution x-ray diffraction and spectroscopic experiments are realized simultaneously).

The dynamic diffraction of x-rays can be realized only in highly perfect crystals. At

the same time, it is well known that ordinarily high-T_c superconductors are not such materials — the acquisition of superconducting properties in materials involves a change in the oxygen composition of the material and is accompanied by the appearance of different defects. Nonetheless, dynamic anomalous transmission of x-rays (Borrmann effect) during Laue diffraction by high-T_c superconducting crystals was observed in Refs. 6 and 7. It is of interest in this connection to determine whether or not the dynamic character of the diffraction is preserved in such a crystal during Bragg reflection. This is not entirely obvious, since the surface region of the crystal (where the wave fields are formed during Bragg diffraction) can be saturated much more strongly by defects than the volume of the crystal as a whole.

Thus our objective in the present work was to observe the dynamic character of Bragg diffraction in the high-T_c superconducting crystal $Nd_{1.85}Ce_{0.15}CuO_{4-\delta}$ according to the form of the secondary-fluorescence yield curve. In the presence of dynamic diffraction, a characteristic minimum and maximum, reflecting the spatial modulation of the amplitude of the electromagnetic field in the volume in the crystal (formation of a standing x-ray wave), should appear in the curve.

Detailed descriptions of the $Nd_{1.85}Ce_{0.15}CuO_{4-\delta}$ samples and their properties are given in Refs. 6 and 7. Topograms indicating the presence of defects and stresses in the crystals are also given there.

The measurements were performed in a double-crystal arrangement with the characteristic Mo$K_{\alpha 1}$ radiation (wavelength $\lambda = 0.7093$ Å, energy $E = 17.4$ keV). A symmetric reflection from a perfect Si(220) crystal was used to monochromatize the incident beam; the interplanar distance for this reflection ($d_{\mathrm{Si}}^{220} = 1.92$ Å) is close to the value for the (006) reflection from the high-T_c superconducting crystal ($d^{006} = 2.03$ Å), which makes it possible to perform measurements in a virtually dispersion-free scheme (the broadening of the reflection curve as a result of dispersion is less than $1''$). Slits were used to cut off the $K_{\alpha 2}$ line and to form a beam with a cross section of 0.1×0.1 mm^2. The high-T_c superconducting crystal with orientation (001) was placed in the reflecting position for the symmetric reflection (006). The yield curves for the characteristic fluorescence radiation NdL_{α} ($E = 5.229$ keV) and NdL_{β_1} ($E = 5.721$ keV) as well as CuK_{α} ($E = 8.040$ keV) and CuK_{β_1} ($E = 8.904$ keV) were recorded.

The results of the measurements and theoretical calculations are presented in Figs. 1a and 1b. The characteristic modulations attesting to the appearance and the interference motion of a standing x-ray wave can be seen in the yield curves of the secondary radiation for both elements. These modulations indicate unequivocally the dynamic character of the diffraction in the sample.

The form of the fluorescence yield curves is determined by the displacement of the antinodes of the standing x-ray wave accompanying a change in the angular position of the crystal relative to the incident beam within the region of total diffraction reflection. The minimum and maximum on the yield curves correspond to different spatial positions of the antinodes of the standing wave with respect to the atoms (minimum — when the atom is located at a node; maximum — when the atom is located at an antinode). The shape of the curve is also affected by extinction associated with a decrease in the effective penetration depth of the incident x-rays during dynamic diffraction.

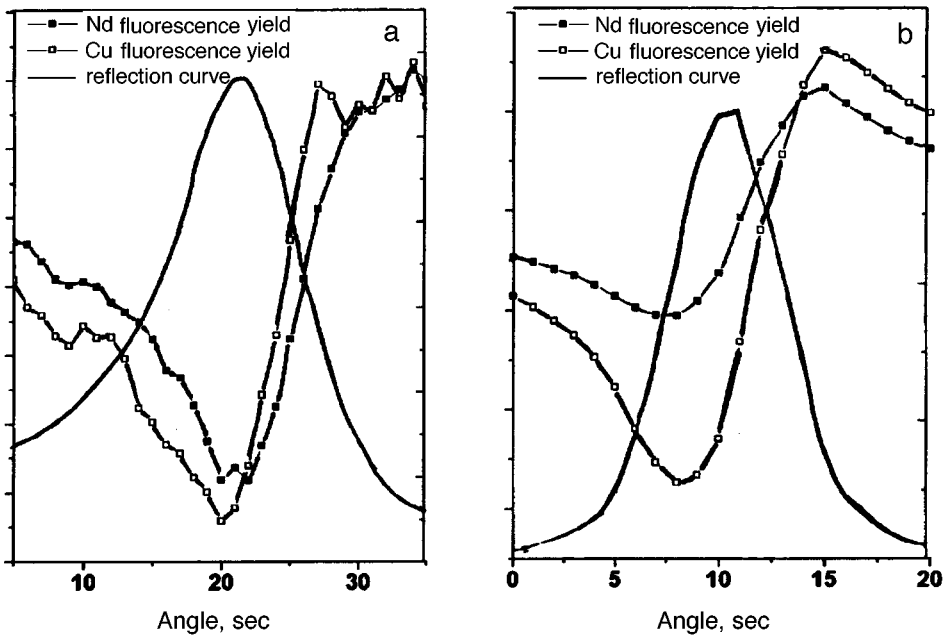

FIG. 1. Experimental (a) and theoretical (b) reflection curves and fluorescence yield from neodymium (L_α–L_{β_1}) and copper (K_α–K_{β_1}) atoms in high-T_c superconducting crystals $Nd_{1.85}Ce_{0.15}CuO_{4-\delta}$.

The fluorescence yield curves are in qualitative agreement with the computational results, despite the fact that the measured width of the reflection curve of the crystal (approximately 22 seconds of arc) is twice the theoretical value. We also note that this difference is much smaller than that observed in Ref. 7, where the measured Laue reflection width was equal to 1.3 minutes of arc, while the theoretical value was 17 seconds. This could indicate either that the surface layers of the sample are less saturated with defects than the deep regions or that the perfection of the crystal can vary substantially from sample to sample.

The positions of the neodymium and copper atoms relative to the diffraction planes for the reflection employed are virtually identical (see Fig. 2a). For this reason, the fluorescence yield curves for these atoms are slightly different. This means that the antinodes and nodes of the standing wave coincide with atoms of both types simultaneously (actually, the differences between the yield curves are due only to the difference in the ratio between the extinction length and the emergence depth of the secondary radiation for different elements). When other reflections, for example (004), are used, the neodymium and copper atoms will be located in different positions relative to the diffraction planes and therefore the corresponding secondary-radiation yield curves will also differ (Fig. 2b).

The observation of the dynamic character of the diffraction of x-rays shows that the method of standing x-ray waves can be used to study the structural features of high-T_c superconducting crystals. However, the low perfection of the material employed, mani-

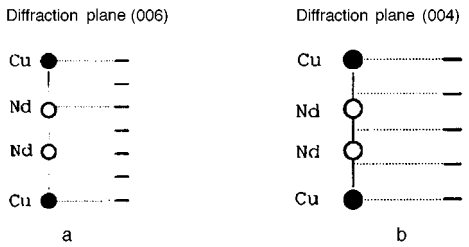

FIG. 2. Schematic diagram of the positions of neodymium and copper atoms in a $Nd_{1.85}Ce_{0.15}CuO_{4-\delta}$ crystal, in projection on the (001) direction, in relation to the diffraction planes for the (006) (a) and (004) (b) reflections.

fested in the large broadening of the reflection curve, makes it much more difficult to obtain the quantitative characteristics. This difficulty can be circumvented by using instead of the standard Bragg diffraction scheme a normal-incidence geometry (as was proposed in Refs. 8 and 9), which can be easily realized using the continuous synchrotron radiation spectrum. In the case of backscattering, the width of the reflection curve is proportional not to χ_{rh} (where χ_{rh} is the real part of the Fourier component of the polarizability for the reciprocal lattice vector employed, $\chi_{rh} \sim 10^{-5}$), as in ordinary diffraction, but rather $(\chi_{rh})^{1/2}$, which increases the width of the reflection curve by an order of magnitude; specifically, the intrinsic width of the (006) reflection which we employed under normal-incidence conditions (realized with incident radiation of energy $E = 3.057$ keV) equals $\sim 1°$. This makes it possible to use the method of standing x-ray waves to study the quantitative characteristics of the structure and defects of crystals with a low degree of perfection (specifically, high-T_c superconducting compounds).

We thank S. I. Zheludeva for helpful discussions in the course of this work. This work was performed under the State program ''Topical problems in condensed-matter physics'' and ''Synchrotron radiation. Beam applications.''

[1] M. V. Koval'chuk and V. G. Kon, Usp. Fiz. Nauk **29**, 63 (1986) [Sov. Phys. Usp. **149**, 426 (1986)].
[2] M. V. Kovalchuk, A. Yu. Kazimirov, and S. I. Zheludeva, Nucl. Instrum. Methods Phys. Res. B **101**, 435 (1995).
[3] J. Bedzyk, G. Materlik, and M. V. Kovalchuk, Phys. Rev. B **30**, N5, 2453 (1984).
[4] S. I. Zheludeva, B. G. Zakharov, M. V. Koval'chuk *et al.*, Kristallografiya **33**, 1352 (1988) [Sov. Phys. Crystallogr. **33**, 804 (1988)].
[5] A. Yu. Kazimirov, M. V. Kovalchuk, A. N. Sosphenov *et al.*, Acta Crystallogr. Sec. B **48**, 577 (1992).
[6] V. V. Kvardakov and V. A. Somenkov, Sverkhprovodimost' **5**(3), 448 (1992) [Superconductivity **5**(3), 442 (1992)].
[7] V. V. Kvardakov, V. A. Somenkov, V. Paulus *et al.*, JETP Lett. **60**, 731 (1994).
[8] T. Ohta, H. Sekiyama, Y. Kitajima *et al.*, Jpn. J. Appl. Phys. **24**, L475 (1985).
[9] J. C. Woicik, T. Kendelewicz, K. E. Miyano *et al.*, Phys. Rev. Lett. **68**, 3414 (1992).

Translated by M. E. Alferieff

Interaction of acoustic and optical branches via a Lifshitz-type invariant

D. G. Sannikov
A. V. Shubnikov Institute of Crystallography, Russian Academy of Sciences, 117333 Moscow, Russia

(Submitted 11 April 1997)
Pis'ma Zh. Éksp. Teor. Fiz. **65**, No. 9, 707–710 (10 May 1997)

It is shown that the interaction of the acoustic and soft optical branches of the spectrum of normal vibrations of a crystal via a gradient invariant of the Lifshitz-invariant type explains the characteristic temperature dependences of these branches as the point of a transition from the initial phase into an incommensurate phase is approached. A comparison is made with the experimental data for betaine calcium chloride dihydrate — BCCD. © *1997 American Institute of Physics.* [S0021-3640(97)00809-8]

PACS numbers: 63.70.+h, 61.44.Fw, 61.50.Ks, 63.20.−e

Among crystals in which a sequence of initial phase (C_0)–incommensurate phase (IC)–commensurate phase (C) phase transitions is observed, the case when the symmetry group of the C_0 phase is D_{2h}^{16} and the modulation vector is directed along one of the three principal directions x, y, or z is often encountered (see, for example, Ref. 1). For definiteness, and for comparison with experiment, this is the case that will be examined below. If the C phase is equitranslational with the C_0 phase, then the order parameter describing the C_0–C phase transition transforms according to the point group D_{2h}. All representations of this group are one-dimensional, and therefore the order parameter has only one component. For this reason a gradient Lifshitz invariant (L invariant), whose presence leads to a sequence of C_0–IC–S phase transitions, does not exist. In Ref. 2 a thermodynamic potential density whose quadratic part has the form

$$\Phi = \alpha\eta^2 + \alpha'\xi^2 + \sigma(\dot{\eta}\xi - \dot{\xi}\eta) + \delta\dot{\eta}^2 + \delta'\dot{\xi}^2 + \kappa\ddot{\eta}^2 + \kappa'\ddot{\xi}^2 \tag{1}$$

was examined in order to explain incommensurate phase transitions in the ferroelectrics thiourea and sodium nitrite.

Here η is the order parameter, which transforms according to one of the vector representations of the group D_{2h}, i.e., as the components of the polarization vector. It can be interpreted as the amplitude of the soft mode belonging to the optical branch of the crystal. An overdot represents a derivative with respect to the coordinate. The variables η and ξ are assumed to be coordinate-dependent; ξ transforms according to a representation of the group D_{2h} which is different from that of η — as a component of the strain tensor.[2]

A distinguishing feature of the potential (1) is the presence of a gradient invariant of the Lifshitz type (LT invariant) with the coefficient σ. It has the same form as the L

invariant (for two-dimensional representations). The variable ξ can be interpreted as the amplitude of a mode belonging to the optical (not soft) branch. Then the two optical branches interact via the LT invariant and the soft branch exhibits the characteristic dispersion form with a minimum at an arbitrary point of the Brillouin zone.[2] However, a second optical branch with the required symmetry may not be present in a particular crystal, but the acoustic branch, which is always present, interacts via the LT invariant with any IR-active optical branch of the crystal (D_{2h} group). The transition from a C_0-phase into an IC-phase will now be determined by the dispersion of the acoustic branch, which has a minimum at an arbitrary point of the Brillouin zone, though the optical branch once again remains soft. This case, which has not been previously investigated but is quite common, will be studied below.

Let the z and y axes be the incommensurate and polar axes, respectively. In the single-harmonic approximation we can write

$$\eta = P_y = \rho \cos qc^*z, \quad \xi = 2u_{yz}/c^* = \dot{u}_y, \quad u_y = \rho' \cos qc^*z, \tag{2}$$

where P_y, $u_{yz,}$ and u_y are components of the polarization vector, the strain tensor, and the displacement vector, respectively. An overdot represents a derivative with respect to zc^*, just as in Eq. (1). Substituting expressions (2) into Eq. (1) and integrating over z we obtain

$$\Phi = \frac{1}{2}(\alpha + \delta q^2 + \kappa q^4)\rho^2 + \sigma q^2 \rho\rho' + \frac{1}{2}(\alpha' + \delta' q^2 + \kappa' q^4)q^2 \rho'^2. \tag{3}$$

Diagonalizing this quadratic form yields an expression for the elastic constants A of the two branches of the spectrum of normal vibrations of the crystal as a function of the dimensionless wave number q:

$$A^2/Y^2 = \frac{1}{2}\{\alpha + (\delta + \alpha')q^2 + (\kappa + \delta')q^4 + \kappa' q^6 \pm [[\alpha + (\delta - \alpha')q^2 + (\kappa - \delta')q^4 - \kappa' q^6]^2 + 4\sigma^2 q^4]^{1/2}\}, \tag{4}$$

where the symbol $\pm$ refers to the optical and acoustic branches, respectively, and Y is a scale factor, determining the arbitrary units in which the values along the A axis are expressed. Since the optical branch is the soft branch, we assume that only the coefficient α depends on the temperature T linearly.

In order to plot expressions (4) we must choose values for the coefficients. This choice will be partially determined by comparing with the experimental data[3] for a betaine calcium chloride dihydrate (BCCD) crystal, which are shown schematically (without experimental points) in Fig. 1. Our problem does not include determining the coefficients in the potential for BCCD, which could be done, thereby obtaining the best agreement between the experimental data (Fig. 2) and the theoretical dependences determined from Eq. (4). For us it is important to obtain only qualitative agreement between these dependences. For this reason we shall simplify the problem as much as possible.

We neglect the dispersion of the acoustic branch, i.e., we set

$$\delta' = 0, \quad \kappa' = 0. \tag{5}$$

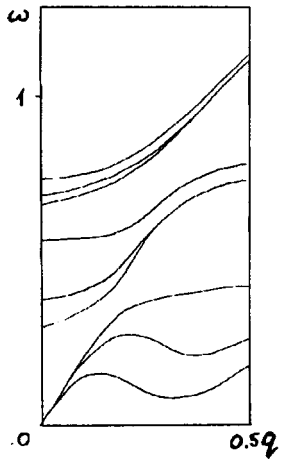

FIG. 1. Three branches of the spectrum in the initial phase of a BCCD crystal for three temperatures (6, 40, and 135 K above $T_i = 164$ K). The dimensionless wave number $q = k/c^*$ and the frequency ω in units of THz are plotted along the abscissa and ordinate, respectively.[3]

As follows from Fig. 1, the experimental dependences correspond approximately to the values

$$q_0^2 = 0.1, \quad \alpha_0 = 0.01, \quad \alpha' = 0.5, \quad Y^2 = 5 \cdot 10^4. \tag{6}$$

Here α_0 is the value of the coefficient α at $T = T_i$, where T_i is the temperature of the C_0–IC phase transition and q_0 is the value of q at the minimum of the acoustic branch at $T = T_i$. The values of the remaining coefficients were chosen as follows:

$$\delta = 0.2, \quad \kappa = 1, \quad \sigma^2 = 0.2. \tag{7}$$

The curves $A(q)$ in Fig. 2, which were constructed according to Eqs. (4)–(7), are displayed for the same values of T as in the caption to Fig. 1, i.e.,

$$\alpha - \alpha_0 = (0.15,\ 1.0,\ 3.2) \cdot 10^{-2}. \tag{8}$$

The value of the coefficient $\alpha_T = 0.04$ in the expression $\alpha = \alpha_T (T - T_i)/T_i + \alpha_0$ is taken from the experimental data on the temperature dependence of the dielectric constant.[4]

Figure 1 contains another optical branch which interacts via the LT invariant with the optical branch examined above. To take this third branch into account, the invariants

$$\alpha'' \zeta^2 + \sigma' (\dot{\eta}\zeta - \dot{\zeta}\eta) + \delta'' \dot{\zeta}^2 + \kappa'' \ddot{\zeta}^2 \tag{9}$$

must be added to Eq. (1). Here the coefficient α'', as one can see from Fig. 1, likewise depends on T but more weakly than does α. If the dispersion and interaction of this branch and the dependence of α'' on T are neglected, i.e., if we set

$$\delta'' = 0, \quad \kappa'' = 0, \quad \sigma' = 0, \quad \alpha'' = \text{const}, \tag{10}$$

then the straight line shown in Fig. 2 ($\alpha'' = 0.07$) is obtained. If simplifying assumptions such as (10) are not used, then better agreement with Fig. 1 can be achieved. It is

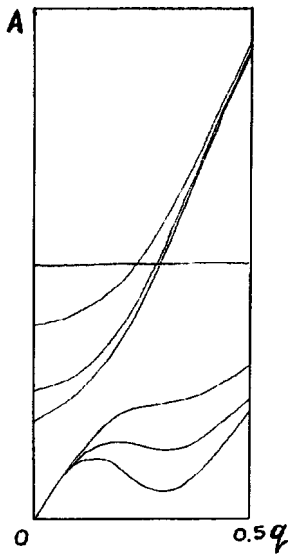

FIG. 2. Three branches, constructed according to Eqs. (4)–(6), of the spectrum of normal vibrations of the crystal for three temperatures (see caption to Fig. 1). The wave number q and the square root of the elastic constants are plotted along the abscissa and ordinate, respectively, in arbitrary units.

sufficient to take account of the interaction ($\sigma' \neq 0$), which makes it impossible for the optical branches to cross and causes them to repel one another as in Fig. 1. We shall not do this. The general character of the curves in Figs. 1 and 2 indicates that the interaction of the acoustic and soft optical branches of the crystal, which are observed experimentally,[3] can be described on the basis of a thermodynamic potential with a LT invariant.

The dispersion of the branches, which is shown in Fig. 2, can be of a different character. For a sufficiently large slope of the acoustic branch, when $\alpha' \geqslant \sigma^2/\delta$, the elasticity of the soft optical mode vanishes at $q=0$, i.e., a direct transition from the C_0 into the C phase occurs. However, once again, the optical and acoustic branches does not cross; the optical branch pushes the acoustic branch downwards near $q=0$ so that the latter branch does not have a minimum. This change in the character of the dispersion of the branches is due to the presence of the Lifshitz point (L point).[5] The coordinates of this point in the (α, α') phase diagram are $\alpha=0$ and $\alpha'=\sigma^2/\delta$. At the L point itself the functions $A(q)$ for small values of q, as follows from Eq. (4), have the form

$$A^2/Y^2=(\delta+\alpha')q^2, \quad A^2/Y^2=2\alpha'\kappa q^4/(\delta+\alpha'), \tag{11}$$

for the soft optical and acoustic branches, respectively.

In the literature one often encounters the assertion that the potential density, which is introduced in Ref. 5, with a single variable η

$$\Phi=\alpha\eta^2-\tilde{\delta}\dot{\eta}^2+\tilde{\kappa}\ddot{\eta}^2+\beta\eta^4 \tag{12}$$

describes the sequence of C_0–IC–C phase transitions no worse than does the potential density (1). This is apparently true if ξ belongs to the optical (not soft) branch. Eliminating formally the variable ξ from Eq. (1), we obtain expression (12) with the coefficients

$$\tilde{\delta} = \sigma^2/\alpha' - \delta, \quad \tilde{\kappa} = \kappa + \sigma^2 \delta'/\alpha'^2 \tag{13}$$

(see, for example, Ref. 6). Now we can forget about the branch which is not soft and study the potential (12) instead of the potential (1), since the C_0–IC phase transition is determined by the dispersion of the soft optical branch, to which the variable η belongs. However, if ξ belongs to the acoustic branch, then the C_0–IC transition is determined by the dispersion of this branch, and it cannot be described on the basis of the potential (12). We note also that the soliton structure of the IC phase, observed experimentally for thiourea, can be explained, as follows from Ref. 7, on the basis of the potential (1) but not the potential (12).

I thank V. A. Golovko for helpful and stimulating discussions, which were largely responsible for the completion of this work.

This work was supported by the Russian Fund for Fundamental Research under Project No. 96-02-18738.

[1] D. G. Sannikov, Kristallografiya **36**, 813 (1991) [Sov. Phys. Crystallogr. **36**, 455 (1991)].
[2] A. P. Levanyuk and D. G. Sannikov, Fiz. Tverd. Tela (Leningrad) **18**, 1927 (1976) [Sov. Phys. Solid State **18**, 1122 (1976)].
[3] H. Quilichini and J. Hlinka, Ferroelectrics **183**, 215 (1996).
[4] H. Wilhelm and H.-G. Unruch, Z. Kristallogr. **195**, 75 (1991).
[5] R. M. Hornreich, M. Luban, and S. Strikman, Phys. Rev. Lett. **35**, 1678 (1975).
[6] D. G. Sannikov, Fiz. Tverd. Tela (St. Petersburg) **38**, 3116 (1996) [Phys. Solid State **38**, 1704 (1996)].
[7] I. Aramburu, G. Madariga, and J. M. Perez-Mato, Phys. Rev. B **49**, 802 (1994).

Translated by M. E. Alferieff

Appearance of new lines and change in line shape in the IR spectrum of a NaV_2O_5 single crystal at a spin-Peierls transition

M. N. Popova[a] and A. B. Sushkov
Institute of Spectroscopy, Russian Academy of Sciences, 142092 Troitsk, Russia

A. N. Vasil'ev
Department of Physics, Moscow State University, 119899 Moscow, Russia

M. Isobe and Yu. Ueda
Institute for Solid State Physics, University of Tokyo, 7-22-1 Roppongi, Minato-ku, Tokyo 106, Japan

(Submitted 15 April 1997)
Pis'ma Zh. Éksp. Teor. Fiz. **65**, No. 9, 711–716 (10 May 1997)

New lines are observed in the infrared spectrum of a crystal due to unit-cell doubling at a spin-Peierls transition (in NaV_2O_5). The change in the shape of the spectral lines at the spin-Peierls transition is recorded. A contour characteristic of a Fano resonance is observed above the transition temperature T_{sp} and the standard symmetric contour is observed below T_{sp}. We attribute this effect to the opening of a gap in the magnetic-excitation spectrum at the spin-Peierls transition. [S0021-3640(97)00909-2]

PACS numbers: 78.30.Er, 75.30.Kz

A number of interesting effects, both of a purely quantum nature and due to the interaction of the magnetic subsystem with lattice deformations, are observed in low-dimensional magnetic systems. Specifically, the magnetic-excitation spectrum of a uniform antiferromagnetic (AF) chain of Heisenberg spins contains a gap in the case of integer spins and no gap in the case of half-integer spins.[1] However, in a real crystal the interaction of one-dimensional magnetic chains of half-integer spins with a three-dimensional phonon field results in dimerization of the atoms in the chains. As a result of such a structural phase transition initiated at the temperature T_{sp} by a spin–phonon interaction, the magnetic-excitation spectrum acquires a gap that separates the nonmagnetic singlet ground state from the first excited triplet state.[2] A transition of this type is the magnetic analog of a Peierls transition in quasi-one-dimensional conductors and, for this reason, it is called a spin-Peierls (SP) transition. A SP transition was first observed in several organic compounds (see, for example, Ref. 2) and then in inorganic transition-metal oxides $CuGeO_3$ (Ref. 3) and NaV_2O_5 (Refs. 4 and 5).

In contrast to their organic analogs, inorganic SP compounds can be obtained in the form of large, high-quality single crystals. This has made it possible to expand the arsenal of methods for investigating the SP transition and to obtain new and fundamental results. For example, for $CuGeO_3$ it is possible to observe the energy gap ($\Delta = 2$ meV)[6] directly by the inelastic neutron scattering method. Magnetic-like excitations with an appreciable

dispersion exist below the SP transition temperature ($T_{sp}=14$ K), while above T_{sp}, all the way up to temperatures close to the temperature of the maximum in the magnetic susceptibility (60 K), magnetic fluctuation modes exist in a wide range of energies.[7] Dimerization of the copper ions along chains has been observed at $T=T_{sp}$, and critical structural fluctuations have been investigated near T_{sp} (see, for example, Ref. 7).

Since dimerization in magnetic chains at a SP transition is accompanied by unit-cell doubling in the direction of the chains, the Brillouin zone (BZ) ''folds'' along this direction, and phonons go from being at the boundary to being at the center of the BZ, in principle making it possible to observe them at $T<T_{sp}$ in the first-order optical spectra. A corresponding change in the spin-excitation spectrum at the SP transition can appear in the ''two-magnon'' spectra. Spectral manifestations of the spin–phonon interaction in the form of asymmetric lines can also be expected in SP systems (Fano resonance[8]). The effects listed above have all been observed[9] in the Raman spectra of $CuGeO_3$. In the present work the appearance of new lines accompanying a SP transition and Fano resonances were observed in the infrared (IR) spectra of SP compounds. A change in spectral line shape at the SP transition was detected.

We investigated the SP vanadate NaV_2O_5, which belongs to the orthorhombic system (space group $P2_1mn$) whose structure contains magnetic and nonmagnetic chains of $V^{4+}O_5$ ($S=1/2$) and $V^{5+}O_5$ ($S=0$) pyramids oriented along the b axis and alternating with one another in the ab layers. The Na atoms lie between the ab layers.[9] The magnetic susceptibility of this compound at temperatures above 35 K is described well by the expression for an antiferromagnetic chain of Heisenberg spins $S=1/2$, coupled by the exchange interaction $\mathcal{H}=\Sigma_i JS_iS_{i+1}$, $J=560$ K,[4] and below 35 K the magnetic susceptibility decreases isotropically.[10] At the same time, new reflections appear in the x-ray scattering.[5] The detailed temperature dependence of the intensity of one reflection gave for the transition temperature $T_{sp}=35.27\pm0.03$ K. At $T=10$ K it was possible to determine the propagation vector for a new superstructure: $\mathbf{q}=(1/2,\ 1/2,\ 1/4)$.

Single crystals, extended along the b axis, with the approximate dimensions $1\times4\times0.5$ mm along the a, b, and c axes, respectively, were obtained in the manner described in Refs. 4 and 5. The orientation of the crystals and the lattice constants ($a=11.318$, $b=3.611$, $c=4.797$ Å) were determined by the x-ray method. We employed samples on which EPR and susceptibility measurements had been performed previously.[10] The IR measurements were performed on plates which 13–20 μm thick in the direction of the c axis. A BOMEM DA3.002 Fourier spectrometer was used to measure the transmission spectra; the measurements were performed at temperatures 5–300 K in the region 50–400 cm^{-1} with a resolution of 0.05–1 cm^{-1}. The samples were placed in a helium atmosphere at a fixed temperature in an optical cryostat with 20-μm thick ''warm'' and ''cold'' mylar windows. To increase the accuracy of the transmission measurements in the temperature range from 300 to 5 K, a special insert in the optical cryostat was fabricated. This insert partially compensated the thermal contraction of the cryostat column and, correspondingly, the motion of the sample, and it also made it possible to register the reference spectrum at any temperature without removing the sample.

The vibrational spectrum of a NaV_2O_5 crystal at $T>T_{sp}$ contains 45 fundamental vibrations: $15A_1+8A_2+7B_1+15B_2$. The A_2 vibrations are inactive in IR absorption. In

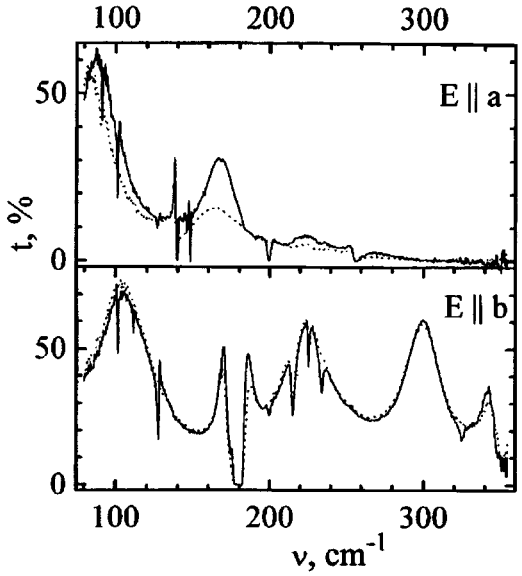

FIG. 1. Transmission spectrum of a NaV_2O_5 single crystal for two polarizations of the light, $\mathbf{E}\|\mathbf{a}$ (top) $T=15$ K$<T_{sp}$ — solid line, $T=38$ K$>T_{sp}$ — dotted line; $\mathbf{E}\|\mathbf{b}$ (bottom) $T=15$ K — solid line, $T=42$ K — dotted line. Spectral resolution: 1 cm^{-1}.

our experimental geometry ($\mathbf{k}\|\mathbf{c}$) A_1 vibrations can appear in $\mathbf{E}\|\mathbf{a}$ polarization and B_1 vibrations can appear for $\mathbf{E}\|\mathbf{b}$. At room temperature two B_1 vibrations ($\nu_{TO}=173$ and 367 cm^{-1}) and two A_1 vibrations ($\nu_{TO}=140$ and 251 cm^{-1}) are seen in the experimental frequency range. The peak at 140 cm^{-1} is strongly asymmetric. As the temperature decreases to 200 K additional lines become visible at the frequencies 168, 215, and 226 cm^{-1} (B_1) and an asymmetric peak appears near 90 cm^{-1} (A_1).

The transmission spectra of a 13-μm thick NaV_2O_5 plate in two polarizations at temperatures above and below T_{sp} are shown in Fig. 1. An intense peak of a B_1 vibration and lines with frequencies 168, 215.1, and 225.7 cm^{-1}, which are probably due to the weakly active B_1 vibrations (the nature of these lines needs to be determined more accurately), are seen in $\mathbf{E}\|\mathbf{b}$ polarization at $T=42$ K against the interference background in the sample. At $T<T_{sp}$ new lines appear and grow at the frequencies 101.5, 117.7, 127, 199.7, 234, and 325 cm^{-1}. The first two lines are very narrow (about 0.2 cm^{-1}), the third line is a doublet (126.7 and 127.5 cm^{-1}) consisting of lines which are just as narrow,[b)] and the remaining lines have a width of about 2 cm^{-1}.

A wide absorption continuum is present in $\mathbf{E}\|\mathbf{a}$ polarization. The intensity of its long-wavelength part decreases appreciably at $T<T_{sp}$. Against the background of this ''bleaching'' of the crystal, the shape of the peaks at 90 and 140 cm^{-1} changes from strongly asymmetric to symmetric. Figure 2 illustrates this for the example of the line with a frequency of about 90 cm^{-1} (the saturation of the line at approximately 140 cm^{-1} at low temperatures distorts its shape). At $T>T_{sp}$ this line possesses a distinct dispersional shape; its width decreases with temperature without a change in shape. At

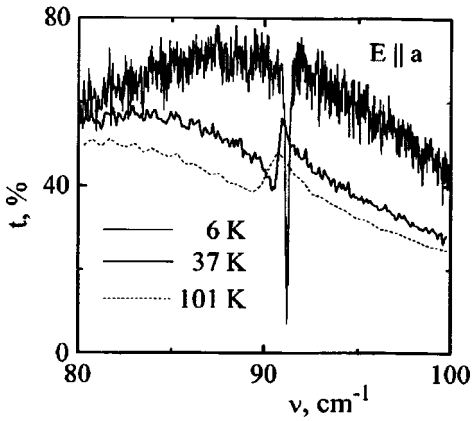

FIG. 2. Line near 90 cm^{-1} in **E**$\|$**a** polarization at temperatures of 101 and 37 K$>T_{sp}$ and 6 K$<T_{sp}$. The spectra were recorded with resolutions (top to bottom) of 0.05, 0.2, and 1 cm^{-1}.

$T<T_{sp}$ a narrow symmetric absorption line is observed at the frequency 91.2 cm^{-1}. At $T<T_{sp}$ new lines appear in the spectrum at the frequencies 101.4, 101.7, 126.8, 127.5, 145.7, 148, 157.2, and 199.5 cm^{-1}. The lines with frequencies below 199 cm^{-1} are very narrow (0.2–0.4 cm^{-1}) and the line at 199.5 cm^{-1} is much wider.[c)]

We shall now discuss our experimental data. According to the x-ray scattering results[5] for NaV_2O_5, at T_{sp} the unit cell doubles in the direction of the *a* and *b* axes and quadruples in the direction of the *c* axis. Hence it follows that at $T<T_{sp}$ phonons from the edges of the BZ become IR active along all directions. The narrow lines which we observed to appear at T_{sp} are evidently due to them. Figure 3 displays the integrated intensity *I* of one such line as a function of the temperature. Since $I\sim\delta^2$, where δ is the displacement of the atoms in the lattice at a structural phase transition (the order param-

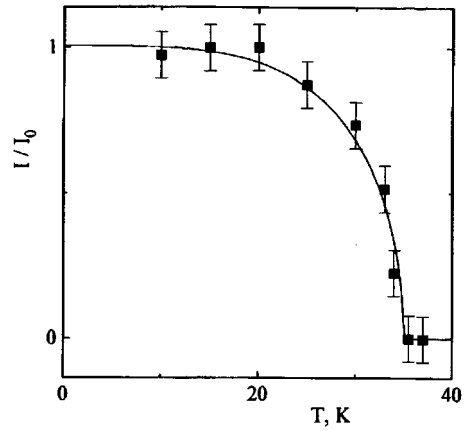

FIG. 3. Temperature dependence of the integrated intensity of a line near 101 cm^{-1} in **E**$\|$**b** polarization.

eter), the function $I(T)$ reflects the temperature variation of the squared order parameter. The accuracy of our measurements is too low for analyzing the applicability of different theories for describing the transition under study.

The absorption continuum observed in $\mathbf{E}\|\mathbf{a}$ polarization is apparently of a magnetic nature. On the basis of the data[4] on the temperature dependence of the magnetic susceptibility of NaV_2O_5, which has a wide maximum near room temperature, it can be concluded that in a quasi-one-dimensional AF spin system short-range order persists right up to room temperature, and therefore magnetic excitations exist.

Wide bands had been observed previously in the absorption spectra of antiferromagnets. They were attributed to photon absorption processes accompanied by the creation of two magnons with equal and oppositely directed wave vectors $\mathbf{q}$ (see, for example, Ref. 11). To find the probability of such a process it is first necessary to examine the interaction of light with a pair of magnetic ions. The analysis for a pair of the nearest magnetic ions V^{4+} in NaV_2O_5 (the symmetry group of the pair is C_s) shows that the first term in the Hamiltonian describing the interaction of the magnetic system with light makes the largest contribution:[11]

$$\mathcal{H}=\sum_i (\mathbf{E}\cdot\boldsymbol{\pi})(\mathbf{S}_i\cdot\mathbf{S}_{i+1}).$$

Here $\mathbf{E}$ is the electric field vector of the light wave; the vector $\boldsymbol{\pi}$ lies in a plane perpendicular to the direction of the spin chain and its magnitude is proportional to the exchange interaction in a spin pair. It is obvious that light polarized perpendicularly to the direction of the chain should be absorbed. The extent of the absorption continuum will be determined by the extent of the magnetic-excitation spectrum and the intensity will be determined by the density of states.

For a uniform Heisenberg chain of $S=1/2$ spins, the magnetic-excitation spectrum extends from 0 to $\nu_m=\pi J$ (if only nearest-neighbor interaction is taken into account).[12] Taking $J=560$ K for NaV_2O_5 (Ref. 4), we find that at $T>T_{sp}$ the absorption continuum extends over approximately 2400 cm^{-1}. At $T<T_{sp}$ the magnetic atoms in the chain dimerize, the chain becomes alternating, and a gap appears in its magnetic-excitation spectrum.[13] According to the inelastic neutron scattering data for NaV_2O_5, the smallest gap opens at the point $\mathbf{q}=(1,1/2,0)$ (the fact that the gap is not located at the center of the BZ is a consequence of the interchain interaction) and its width is $\Delta=9.8$ meV $=79$ cm^{-1} (Ref. 5). In this case the continuum of two-magnon excitations at $T<T_{sp}$ starts above $2\Delta=158$ cm^{-1}. A feature due to the density of states near the gap can be expected to appear at the frequency $\nu=2\Delta$.

The behavior of the absorption continuum in the IR spectra agrees qualitatively with the picture described above: The continuum is observed only in $\mathbf{E}\|\mathbf{a}$ polarization, and below the SP transition temperature the intensity of its long-wavelength part decreases. At $T<T_{sp}$, a weak line is present at the frequency $\nu=157.2$ $cm^{-1}\simeq 2\Delta$. However, it does not shift as $T\to T_{sp}$, so that it cannot be attributed to a gap-associated feature.

The interaction of the lattice vibrations with the magnetic-excitation continuum is manifested in the asymmetric line shape that is characteristic for a Fano resonance.[8] Such a line against the continuum background is shown in Fig. 2 for temperatures 101 K,

37 K$>T_{sp}$. As a result of the change in the magnetic-excitation spectrum at the SP transition, the spin–phonon interaction and hence the line shapes change. The most striking manifestations of this effect should be expected at low frequencies, where below T_{sp} the continuum vanishes on account of the opening of the gap in the magnetic-excitation spectrum. This vanishing of the continuum at $T<T_{sp}$ and the associated transformation of the line shape from a Fano dispersion contour to an ordinary symmetric absorption contour are clearly seen in Fig. 2.

A more detailed investigation of the effects observed requires data on the dispersional dependences of the phonon and magnetic-excitation energies in NaV_2O_5. Such data do not exist at present.

We thank E. A. Vinogradov, O. N. Kompants, and G. M. Zhizhin for assisting in this work. This work was supported by the Russian Fund for Fundamental Research under Grants Nos. 95-02-03796-a and 96-02-19474.

[a)]e-mail: popova@alpha.isan.troitsk.ru
[b)]One component of the doublet is saturated, which can distort the recorded line shape.
[c)]This line is close to saturation, and for this reason its width cannot be determined correctly.

[1]F. D. M. Haldane, Phys. Rev. Lett. **50**, 1153 (1983).
[2]A. I. Buzdin and L. N. Bulaevskiĭ, Usp. Fiz. Nauk **131**, 495 (1980) [Sov. Phys. Usp. **23**, 409 (1980)].
[3]M. Hase, I. Terasaki, and K. Uchinokura, Phys. Rev. Lett. **70**, 3651 (1993).
[4]M. Isobe and Y. Ueda, J. Phys. Soc. Jpn. **65**, 1178 (1996).
[5]Y. Fujii, H. Nakao, T. Iosihama *et al.*, Tech. Report ISSP, Ser. A, No.3171 (1996).
[6]M. Nishi, O. Fujita, and J. Akimitsu, Phys. Rev. B **50**, 15412 (1995).
[7]K. Hirota, G. Shirane, Q. J. Harris *et al.*, Phys. Rev. B **52**, 1866 (1995).
[8]U. Fano, Phys. Rev. B **124**, 1866 (1961).
[9]A. Carpy and J. Galy, Acta Crystallogr. Sec. B **31**, 1481 (1975).
[10]A. N. Vasil'ev, A. I. Smirnov, M. Isobe, and Y. Ueda, submitted to Phys. Rev. B
[11]T. Moriya, J. Appl. Phys. **39**, 1042 (1968).
[12]G. Müller, H. Thomas, H. Beck, and J. C. Bonner, Phys. Rev. B **24**, 1429 (1981).
[13]J. C. Bonner and H. W. J. Blöte, Phys. Rev. B **25**, 6959 (1982).

Translated by M. E. Alferieff

Transverse spin dynamics of a spin-polarized Fermi liquid

I. A. Fomin

P. L. Kapitsa Institute of Physics Problems, Russian Academy of Sciences, 117334 Moscow, Russia

(Submitted 16 April 1997)
Pis'ma Zh. Éksp. Teor. Fiz. **65**, No. 9, 717–721 (10 May 1997)

A microscopic derivation of the equations of transverse spin dynamics of a spin-polarized Fermi liquid at zero temperature is given in the leading-order approximation in the frequencies and wave vectors characterizing the spin motion. The equations are applicable for arbitrary degree of polarization and arbitrary deviations of the spin direction from the equilibrium orientation. The solutions describing a coherently precessing two-domain structure and spin waves are examined. In contrast to the assertion discussed in the literature that spin waves are damped at zero temperature, spin waves are found to be undamped in the long-wavelength limit. © *1997 American Institute of Physics.* [S0021-3640(97)01009-8]

PACS numbers: 71.10.Ay, 74.20.Mn

1. Substantial progress has been made in recent years in the preparation and experimental investigation of strongly polarized Fermi liquids. The objects of study are pure liquid ^{3}He and liquid solutions of ^{3}He in ^{4}He. For the polarizations achieved the change in the distribution function of the Fermi quasiparticles cannot be treated as small and the Landau Fermi liquid theory is literally inapplicable. Specifically, this refers to the equations governing the spin dynamics of such a liquid — the Leggett equations.[1] The need for changes is already evident from the fact that in a polarized system there are two different Fermi momenta p_{F+} and p_{F-} for the quasiparticles with spin directed parallel and antiparallel to the total spin, respectively. As a result, the Fermi liquid parameters appearing in the Leggett equations no longer have a definite meaning. A more serious difficulty is also discussed in the literature — the so-called zero-temperature damping of transverse spin disturbances.[2–4] The formal difficulty lies in the fact that when the direction of the spin changes, the state of the Fermi quasiparticles changes in the entire range from p_{F-} to p_{F+}. In addition, the quasiparticle decay probability increases with polarization as $(p_{F+}-p_{F-})^2/p_F^2$, and for a high degree of polarization the reciprocal of the lifetime of the quasiparticles is found to be comparable to their energy. A microscopic theory, whose goal is to overcome this difficulty, has been proposed in a series of works.[4] According to these works, taking account of the possibility of quasiparticle decay has the effect that the transverse components of the spin-diffusion temperature and the damping of spin waves remain finite right down to zero absolute temperature.

In the present letter the equations of spin dynamics are derived directly at $T=0$. It is found that an expansion in the reciprocal of the polarization is possible. The leading

terms in the frequencies and wave vectors characterizing the spin motion are retained. The equations obtained in this manner are nondissipative. Specifically, spin waves are undamped in the leading long-wavelength approximation. This result agrees with the theory of a ferromagnetic Fermi liquid[5] and does not agree with the results obtained in Refs. 2 and 4.

2. DERIVATION OF THE EQUATIONS

The Hamiltonian of the Fermi liquid under study includes the kinetic energy $\mathcal{H}_{\rm kin}$, the two-particle interaction $\mathcal{H}_{\rm int}$, and the interaction $\mathcal{H}_L = -\omega_L S_z$ with a magnetic field oriented along the z axis, where S_z is the z projection of the spin density and ω_L is the Larmor frequency corresponding to the field. In both ^{3}He and solutions of ^{3}He in ^{4}He the spin–orbit interaction is very weak and we shall neglect it. We introduce at each point a coordinate system rotating with angular velocity Ω such that the polarization in the rotating system is the locally equilibrium polarization. Then Ω depends on the time and the coordinates. If this dependence is slow, i.e., the frequencies ω and wave vectors $\mathbf{k}$ characterizing the change in Ω in a coordinate system rotating with the Larmor frequency satisfy the strong inequalities $\omega \ll \Omega$ and $k \ll \Delta p = p_{F+} - p_{F-}$, then an expansion in small frequencies and wave vectors, similar to the method employed previously[6] for the B-phase of ^{3}He, can be used to derive the spin-dynamics equations. We shall proceed from the Lagrangian $\hat{\mathcal{L}} = i(\partial/\partial t) - \hat{\mathcal{H}}$, written in the second-quantization representation

$$\hat{\mathcal{L}} = \frac{1}{2}\int \psi\dagger_\mu(\mathbf{r})\left[\delta_{\mu\nu} i\frac{\partial}{\partial t} + \sigma^z_{\mu\nu}\cdot\omega_L - \sigma_{\mu\nu}\cdot\Omega\right]\psi_\nu(\mathbf{r})d^3r - \frac{1}{2m}\int [\nabla\psi\dagger_\mu(\mathbf{r})] \times [\nabla\psi_\mu(\mathbf{r})]d^3r - \hat{\mathcal{H}}_{\rm int}. \quad (1)$$

Let us perform a local rotation (specified by the Euler angles α, β, and γ) of the spin axes $\hat{x}$, $\hat{y}$, $\hat{z}$ so that at each point the new spin quantization axis $\hat{\xi}$ is directed along Ω. The condition on the orientation of the axes $\hat{\xi}$ and $\hat{\eta}$ will be formulated below. This rotation results in a ''stretching'' of the spatial and time derivatives in Eq. (1) according to the rule

$$\delta_{\mu\nu}\frac{\partial}{\partial t} \to \delta_{\mu\nu}\frac{\partial}{\partial t} + R\dagger_{\mu\lambda}\frac{\partial}{\partial t}R_{\lambda\nu}$$

and similarly for the gradients. The rotation matrix $\hat{R}$ is defined as

$$\hat{R} = \exp(-\gamma\hat{\sigma}^z/2)\exp(-\beta\hat{\sigma}^y/2)\exp(-\alpha\hat{\sigma}^z/2).$$

As a result of this stretching, the Lagrangian acquires additional terms containing time derivatives $\dot{\alpha}$, $\dot{\beta}$, and $\dot{\gamma}$ and spatial derivatives α_l, β_l, and γ_l, where the index designates differentiation with respect to the lth coordinate, of the Euler angles. It is convenient to combine with $\hat{\mathcal{H}}_L$ the correction arising from the stretching of the time derivative. As a result we obtain

$$\hat{\mathcal{L}}_1 = \frac{1}{2}\int \psi\dagger_\mu(\mathbf{r})(\sigma_{\mu\nu}\cdot\omega)\psi_\nu(\mathbf{r})d^3r, \quad (2)$$

where ω has the following projections on the rotated axes:

$$\omega_\xi = -(\dot{\alpha}+\omega_L)\sin\ \beta\ \cos\gamma + \dot{\beta}\ \sin\gamma,$$

$$\omega_\eta = (\dot{\alpha}+\omega_L)\sin\ \beta\ \sin\gamma + \dot{\beta}\ \cos\gamma,$$

$$\omega_\zeta = \dot{\gamma} + (\dot{\alpha}+\omega_L)\cos\beta. \tag{3}$$

The spatial derivatives are collected in

$$\hat{\mathcal{L}}_2 = \frac{1}{2m}\int \{\partial_l \psi\dagger_\mu(\mathbf{r})(A_a^l \sigma_{\mu\nu}^a)\psi_\nu(\mathbf{r}) - \psi\dagger_\mu(\mathbf{r})(A_a^l\sigma_{\mu\nu}^a)\partial_l\psi_\nu(\mathbf{r})$$
$$+ \psi\dagger_\mu(\mathbf{r})\psi_\mu(\mathbf{r})A_a^l A_a^l\} d^3r, \tag{4}$$

where A_a^l are the spin or ''chiral'' velocities

$$A_\xi^l = -\alpha_l\ \sin\ \beta\ \cos\gamma + \beta_l\ \sin\gamma,$$

$$A_\eta^l = \alpha_l\ \sin\ \beta\ \sin\gamma + \beta_l\ \cos\gamma,$$

$$A_\zeta^l = \gamma_l + \alpha_l\ \cos\ \beta. \tag{5}$$

The remaining freedom in the orientation of a local reference frame can be used to make the transport velocity A_η^l of the longitudinal spin component vanish:

$$\gamma_l + \alpha_l\ \cos\ \beta = 0. \tag{6}$$

The expression for the spin-current operator $\hat{j}_a^l(\mathbf{r})$ is obtained by varying $\hat{\mathcal{L}}_2$ with respect to A_a^l by virtue of the definition $\delta\hat{\mathcal{L}}_2 = \int \hat{j}_a^l \delta A_a^l d^3r$. After transformations, the total Lagrangian $\hat{\mathcal{L}}$ will have the form

$$\hat{\mathcal{L}} = \hat{\mathcal{L}}_0 + \hat{\mathcal{L}}_1 + \hat{\mathcal{L}}_2. \tag{7}$$

where $\hat{\mathcal{L}}_0$ is the Lagrangian of the Fermi liquid in a uniform field Ω directed along the ζ axis. The ground state for $\hat{\mathcal{L}}_0$ corresponds to $\langle \hat{S}_\zeta \rangle = S$, $\langle \hat{S}_\xi \rangle = 0$, and $\langle \hat{S}_\eta \rangle = 0$. The derivatives α_l, β_l, γ_l, $\dot{\beta}$, and $\dot{\gamma}$ and the combination $\dot{\alpha}+\omega_L$ are small in the sense indicated above and the sum $\hat{\mathcal{L}}_1 + \hat{\mathcal{L}}_2$ is an adiabatic perturbation which does not give rise to transitions to excited states. A change in state can occur only as a result of a change in the spin orientation relative to stationary axes, which is given by the angles α and β according to the relations $S_x = S\sin\beta\ \cos\alpha$, $S_y = S\sin\beta\ \sin\alpha$, and $S_z = S\cos\beta$. The first-order correction to the averaged Lagrangian contains only the time derivatives of the angles. To take account of the terms with spatial derivatives, the second-order correction must be calculated according to the well-known scheme given in Ref. 6. The sum of both corrections is a Lagrangian characterizing the motion of the spin S in leading order in ω and k:

$$\mathcal{L} = S[(\dot{\alpha}+\omega_L)\cos\beta + \dot{\gamma}] + \frac{1}{2}\chi_\perp^J(\alpha_l^2\sin^2\beta + \beta_l^2). \tag{8}$$

The coefficient $\chi_\perp^J$ in this formula is the transverse component of the static current susceptibility. The current susceptibility $(\chi^J)_{ab}^{lm}(\omega, \mathbf{k})$ is the tensor coefficient in the

linear relation between the Fourier components of the spin current and the chiral velocity $j_a^l = \chi_{ab}^{lm} A_b^m$. In expression (8) the susceptibility $\chi_\perp^J$ is the coefficient of the second-order terms in k, so that its value for $\omega = 0$ and $k = 0$ can be used. Because the spin–orbit interaction is small, the static susceptibility is isotropic with respect to the spatial indices l and m. With respect to the spin indices this is a uniaxial tensor, and its component along the spin does not appear in the expression for $\mathcal{L}$ because of the condition (6). By virtue of the general properties of the susceptibility $\chi_\perp^J(0,0)$ is a real number. The components of the tensor $(\chi^J)_{ab}^{lm}(\omega, \mathbf{k})$ can be expressed in terms of the Fourier transforms of the retarded commutators of the corresponding components of the spin current (see Ref. 6). These commutators cannot be calculated in the general case. In the weak-polarization limit the Fermi-liquid theory gives $\chi_\perp^J(0,0) = (\hbar/2)^2 N(0)(v_f^2/3\Lambda)$, where Λ is a combination of Fermi-liquid parameters, $\Lambda = 1/(1+F_0^a) - 1/(1+F_1^a/3)$.

The Lagrangian (8) engenders the following equations of motion:

$$\frac{\partial S}{\partial t} = 0, \tag{9}$$

$$\frac{\partial}{\partial t}(S\cos\beta) + \chi_\perp^J \frac{\partial}{\partial x_l}(\alpha_l \sin^2\beta) = 0, \tag{10}$$

$$S\sin\beta\left(\frac{\partial \alpha}{\partial t} + \omega_L\right) - \chi_\perp^J[(\nabla\alpha)^2 \sin\beta\cos\beta - \Delta\beta] = 0. \tag{11}$$

Here Δ is the Laplacian. Equations (9)–(11) are identical to the equations governing the spin dynamics of an isotropic ferromagnet[7] written in terms of the Euler angles. By virtue of Eq. (9) one has $S =$ const. The change in the orientation of S is determined by Eqs. (10) and (11).

Let us now examine the simple stationary solutions of these equations. In a constant and uniform magnetic field we have a solution of the form β=const, $\nabla\alpha = \mathbf{k}$, $\dot{\alpha} = -\omega_\mathbf{p}$. Substituting this solution into Eq. (11) we obtain

$$\omega_p = \omega_L - \frac{\chi_\perp^J}{S} k^2 \cos\beta. \tag{12}$$

For small β, setting $\cos\beta \approx 1$, we obtain a standard spin wave with a quadratic dispersion law. In the leading long-wavelength approximation under consideration here, the wave is undamped. Kondratenko[5] showed that in a ferromagnetic Fermi liquid the damping of spin waves arises only in terms of order $\sim k^5$. His arguments, which are based on an estimate of the phase volume for different spin-wave decay processes, are also applicable to a polarized Fermi liquid.

The expression (12) makes it possible to indicate more accurately the region of applicability of the approach employed. From the condition of adiabaticity $(\omega_p - \omega_L) \ll \Omega$ follows the bound $(\chi_\perp^J/S)k^2 \ll \Omega$. For weak polarization $\chi_\perp^J$ can be expressed in terms of the parameters of the Fermi liquid, which gives $kv_F/\Omega \ll \sqrt{3\Lambda/(1+F_0^a)}$. In pure ^{3}He the right-hand side of the inequality is ~ 1 and we return to the criterion $kv_F/\Omega \ll 1$. In solutions $\Lambda \ll 1$ and the restriction is more stringent:

$kv_F/\Omega \ll \sqrt{3\Lambda}$. For $kv_F/\Omega \sim \sqrt{\Lambda}$ spin waves interact efficiently with the longitudinal degree of freedom and the separation into longitudinal and transverse dynamics is no longer justified.

Another solution of Eqs. (10) and (11) which is of interest arises in a weakly nonuniform field, when $\omega_L = \omega_L(z)$: $\dot{\beta} = 0$, $\dot{\alpha} = -\omega_p$, and $\alpha_l = 0$. The change in the angle β, according to Eq. (11), is described by the equation

$$\chi_\perp^J \frac{\partial^2 \beta}{\partial z^2} + S \frac{d\omega_L}{dz}(z - z_0)\sin\beta = 0. \tag{13}$$

This equation has the same form as a previously studied[8] equation describing a coherently precessing spin structure in a weakly polarized Fermi liquid. This shows that a coherently precessing structure should also exist in a strongly polarized Fermi liquid. The equation (13) does not take into account the effect of demagnetizing fields, which in the case of spin polarization can be significant. This can be done directly.[9]

3. DISCUSSION

On the basis of its symmetry properties, a Fermi liquid with ''frozen'' polarization is similar to an isotropic ferromagnet. Therefore it is not surprising that the equations governing the spin dynamics of such a liquid are identical to the analogous equations for a ferromagnet. The same result is obtained by passing in the Leggett equations to the limit $\Omega\tau \to \infty$ and correspondingly redefining the coefficients in the equations. This justifies the use of the Leggett equations in the indicated limit in the case of strong polarization as well. This is not true of the dissipative terms. To introduce dissipation, terms with higher powers of the frequencies and wave vectors must be included in the equations. However, taking into account dissipation cannot eliminate the discrepancy concerning the question of the zero-temperature damping, since the discrepancy arises even in terms of order k^2. Measurements of the diffusion coefficient in pure polarized ^{3}He (Ref. 10) and in solutions of ^{3}He and ^{4}He (Ref. 11) show a substantial decrease in the transverse component of the diffusion coefficient compared with the longitudinal component at temperatures $T \leqslant \Omega$. This agrees qualitatively with the idea of zero-temperature damping. However, the experimental results obtained cannot be regarded as a direct proof of the existence of such damping. A calculation of the diffusion coefficient requires analysis of the interaction of all elementary excitations contributing to spin transport, i.e., Fermi quasiparticles and spin waves. The presence of two types of excitations can result in the existence of regions with different temperature dependences. Changes in the character of the transverse spin diffusion in the region $T \sim \Omega$ can be expected in different specific models of the phenomenon. A final conclusion about the experimental confirmation of the existence of zero-temperature damping can be made only after the corresponding calculations are performed.

I thank A. F. Andreev, V. V. Dmitriev, and P. S. Kondratenko for helpful discussions. This work was supported in part under CRDF Grant No. RP1-249.

[1] A. J. Leggett, J. Phys. C **3**, 448 (1970).
[2] A. E. Meyerovich, Phys. Lett. A **107**, 177 (1985).
[3] J. W. Jeon and W. J. Mullin, J. Low Temp. Phys. **49**, 421 (1987); Phys. Rev. Lett. **62**, 2691 (1989); J. Low Temp. Phys. **88**, 433 (1992).
[4] A. E. Meyerovich and K. A. Musaelian, J. Low Temp. Phys. **89**, 781 (1992); J. Low Temp. Phys. **94**, 249 (1994); J. Low Temp. Phys. **95**, 789 (1994); Phys. Rev. Lett. **72**, 1710 (1994).
[5] P. S. Kondratenko, Zh. Éksp. Teor. Fiz. **46**, 1438 (1964) [Sov. Phys. JETP **19**, 972 (1964)].
[6] K. Maki, Phys. Rev. B **11**, 4264 (1975).
[7] L. Landau and E. Lifshitz, Phys. Z. Sowjetunion **8**, 153 (1935).
[8] V. V. Dmitriev and I. A. Fomin, JETP Lett. **59**, 378 (1994); I. A. Fomin, Physica B **210**, 373 (1995).
[9] I. A. Fomin and G. Vermeulen, J. Low Temp. Phys. **106**, 133 (1997).
[10] L.-J. Wei, N. Kalenchofsky, and D. Candela, Phys. Rev. Lett. **71**, 879 (1993).
[11] J. H. Ager, A. Child, R. Konig *et al.*, J. Low Temp. Phys. **99**, 683 (1995).

Translated by M. E. Alferieff

Shock wave structure in simple liquids

S. I. Anisimov,[a)] V. V. Zhakhovskiĭ,[b)] and V. E. Fortov
Landau Institute for Theoretical Physics, Russian Academy of Sciences, 117334 Moscow, Russia

(Submitted 10 April 1997)
Pis'ma Zh. Éksp. Teor. Fiz. **65**, No. 9, 722–727 (10 May 1997)

The shock wave structure in a liquid is studied by a molecular dynamics simulation method. The interaction between atoms is described by the Lennard–Jones (6–12) potential. In contrast to earlier works, the simulation is performed in a reference frame tied to the shock wave front. This approach reduces non-physical fluctuations and makes it possible to calculate the distribution functions of the kinetic and potential energy for several cross sections within the shock layer. The profiles of flow variables and their fluctuations are found. The surface tension connected with pressure anisotropy within the shock front is calculated. It is shown that the main contribution to the surface tension coefficient comes from the mean virial. © *1997 American Institute of Physics.* [S0021-3640(97)01109-2]

PACS numbers: 02.70.Ns, 62.50.+p

The internal structure of shock waves has been extensively investigated, both experimentally and theoretically (see, e.g., Refs. 1–13). Earlier theoretical studies of shock wave structure were based either on the hydrodynamic approximation (which is valid for weak shock waves only)[2–5] or on the Boltzmann kinetic equation (which holds for rarefied gases only).[6–8] Thus, only certain limiting cases have been studied. More recently, the direct Monte Carlo and molecular dynamics (MD) simulation methods have been employed to study the shock wave structure in solids, liquids, and dense gases (see Refs. 9–13). However, those simulations all suffer from large nonphysical fluctuations, which have until now prevented the study of such important characteristics of the shock layer as the evolution of velocity distribution function across the layer. There are two main reasons for the high level of fluctuations in the MD shock wave simulations. First, in most of these simulations a standard statement of the problem is used, wherein a shock wave is generated in a fluid at rest by a moving piston. As a result, the shock wave is nonstationary in the laboratory frame. Second, the number of particles in the MD cell is typically of the order of a few thousand, which is insufficient for quantitative description of the shock wave structure. In the present work we use a special potential configuration that makes it possible to generate a shock wave at rest in the laboratory frame, and employ the so-called Langevin thermostat to create the upstream fluid flow with given mass velocity and temperature. The number of atoms in our simulations was typically an order of magnitude larger than in Refs. 10, 11, and 13. This approach substantially improves the quality of simulation and allows us to trace the evolution of the kinetic and potential energy distributions across the shock layer. Since the kinetic energy distribution

within the shock layer is nonequilibrium, the concept of local temperature is not applicable. In this work we use the mean-square fluctuations of the longitudinal and transverse velocity components to describe the transformation of kinetic energy of the upstream flow into thermal energy of the downstream flow. We employ also the pair correlation function (which depends on the transverse coordinates (x,y)), calculated for several planes $z=$ const within the shock layer, to describe the evolution of the fluid structure during the shock compression.

The interaction of atoms in a simple liquid is described in this work by the Lennard–Jones (6–12) potential (LJ potential):

$$U(r)=4\varepsilon[(\sigma/r)^{12}-(\sigma/r)^{6}]. \tag{1}$$

We will hereafter use the MD units defined in terms of the parameters of the potential (1). The results of the calculations will then be valid for any LJ fluid. The parameter σ is chosen as the unit of length, and the parameter ε as the unit of energy. It is convenient to chose the particle mass equal to 48 MD units. The units of time and velocity are then $\sigma\sqrt{m/48\varepsilon}$ and $\sqrt{48\varepsilon/m}$, respectively. For example, for argon atoms, the unit of length is $\sigma=0.3405$ nm, the unit of time is 0.31144 ps, the unit of energy (temperature) is $\varepsilon=1.654\cdot 10^{-14}$ erg $=119.8$ K, the unit of velocity is 1.0933 km/s, and the unit of density is 1.6825 g/cm^3. The rectangular MD simulation cell is similar to that used in our previous paper.[14] It has the dimensions $L_x\times L_y\times 2L_z$ with periodic boundary conditions imposed along all three coordinate axes. The flow velocity is directed along the z axis. Short-range potentials U^+ and U^- are located on opposite sides of the MD cell and satisfy the condition that the forces $\partial U^+/\partial z=\partial U^-/\partial z=0$ at $z=\pm L_z$. Since the accelerating U^+ and decelerating U^- potentials have different magnitudes, the atoms crossing the boundary of the MD cell change their energy. To form a uniform upstream flow with given temperature T_1 and mass velocity $V_1=V_{1z}$, the Langevin thermostat[15] is used. The thermostat is a part of the MD cell in which the atoms are subjected to the Langevin force

$$dv_i^a/dt=\beta(V_1\delta_{iz}-v_i^a)+\xi_i(t), \tag{2}$$

where β is the friction coefficient, $\xi_i(t)$ is Gaussian random force (''white noise''), the subscript $i=x,y,z$, and the superscript a numbers the atoms. To obtain a prescribed temperature T_1, the parameters of Eq. (2) should satisfy the condition $\langle\xi_i^2\rangle=2\beta T_1/\Delta t$, where Δt is the time step of the integration, and the temperature is expressed in energy units. The equations of motion are integrated using the 8th order Stoermer method, which was previously used in Refs. 14, 16, and 17 for MD simulation of shock waves in L-J gases and the liquid–gas phase transition. The details of the algorithm are described in Ref. 14.

TABLE I.

$\lvert V_1\rvert$	$\lvert V_2\rvert$	n_1	n_2	T_1	T_2	l_s	γ_T	γ_u	γ
2.48	1.61	0.76	1.17	1.03	7.86	1.95	5.90	40.93	46.83
4.95	2.74	0.76	1.37	1.04	48.65	1.42	49.36	120.14	169.50

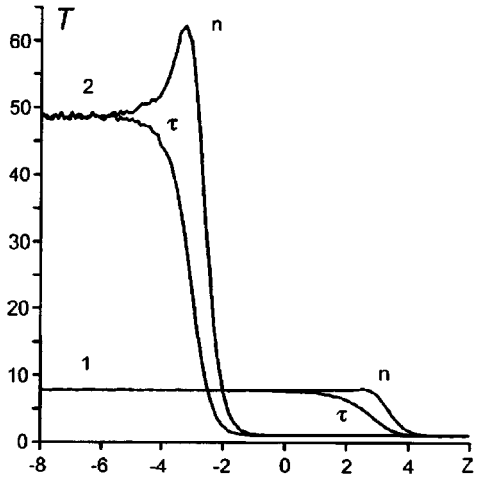

FIG. 1. Spatial profiles of the mean-square fluctuations of the longitudinal (n) and transverse (τ) velocity components in stationary shock waves. Upstream velocities are: curve *1*) $|V_1|=2.48$ and curve *2*) $|V_1|=4.95$.

Let us consider some typical examples of such a simulation. The parameters of shock waves for two different Mach numbers ($M\approx|V_1|$ for liquid argon) are presented in Table I.

The shock wave thickness presented in Table I is defined as

$$l_s=(n_2-n_1)/(dn/dz)_{\max}.$$

Figure 1 shows the profiles of the mean-square fluctuations of the longitudinal (curve n) and transverse (curve τ) components of the molecular velocity. The simulation reveals that the fluctuation of the longitudinal velocity component, $T_n=48\langle(v_z-\overline{v_z})^2\rangle$, grows faster than the fluctuation of the transverse component, $T_\tau=48\langle v_x^2\rangle$. A similar phenomenon has been observed in dense gases.[16] It can be attributed to the fact that the transformation of the energy of ordered motion along the z axis into energy of random (thermal) motion along the x and y axes requires large-angle scattering. This transformation proceeds slowly since it is connected with the high-energy tail of the particle distribution. In contrast, the analogous process resulting in thermalization of the z component of the velocity has little to do with the tail of the distribution function and has a higher rate. Note that the function $T_n(z)$ has a maximum within the shock front at sufficiently high Mach number. The difference between T_n and T_τ leads to anisotropy of the pressure within the shock layer and to an effect similar to surface tension. The pressure in the case under consideration is a symmetric tensor, rather than a scalar. In the general nonequilibrium case the pressure tensor can be calculated using the procedure described in Refs. 18 and 19 and the results of the MD simulation. The components of pressure are given by

$$P_n(z)=n(z)T_n(z)-\frac{1}{2S}\left\langle\sum_{a\neq b}\frac{z_{ab}^2}{r_{ab}}\frac{\partial U(r_{ab})}{\partial r_{ab}}\delta(z-z_a)\right\rangle, \tag{3a}$$

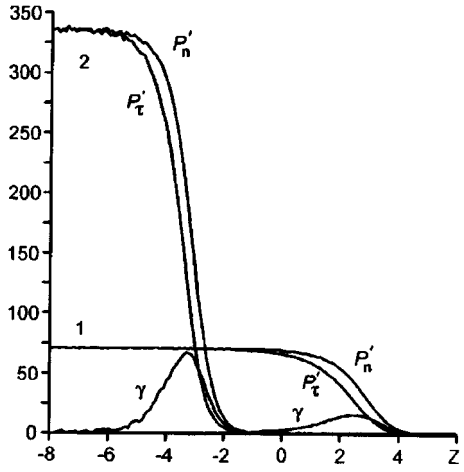

FIG. 2. Spatial profiles of the normal (n) and tangential (τ) pressure components in stationary shock waves.

$$P_\tau(z)=n(z)T_\tau(z)-\frac{1}{2S}\left\langle \sum_{a\neq b}\frac{(x_{ab}^2+y_{ab}^2)}{2r_{ab}}\frac{\partial U(r_{ab})}{\partial r_{ab}}\delta(z-z_a)\right\rangle, \tag{3b}$$

where S is the area of the MD cell in the x,y plane. The coefficient of surface tension is defined as

$$\gamma=\int_{-\infty}^{\infty}(P_n-P_\tau)dz. \tag{4}$$

The virial terms of the normal and tangential components of the pressure P_n and P_τ and the difference between them $\gamma(z)$ are calculated in the same way as in Ref. 16 and are presented in Fig. 2. Notice that in the case of liquids the main contribution to γ originates from the potential energy of particle interaction (second terms in Eqs. (3a) and (3b)), whereas in gases it is connected with the kinetic energy of the particles (the first terms in Eqs. (3a) and (3b)).[16,20] The values of the ''potential'' (γ_u) and ''kinetic'' (γ_T) contributions to the surface tension γ are given in Table I. As is clear from Eq. (4), the surface tension is a small effect, proportional to the shock wave thickness. The corresponding correction to the downstream pressure P_2 is of the order of $P_2 l_s/R$, where R is the radius of curvature of the shock wave. The excess pressure behind a spherical shock front observed in Ref. 21 may be attributed to the surface tension (see Ref. 20).

The effect of surface tension may play an important role in the problem of shock wave stability. For a plane shock wave, considered as a gasdynamic discontinuity, the problem of stability with respect to corrugation perturbations was first considered in Ref. 22. The analysis showed that, depending on slope of the Hugoniot curve, the wave may be stable, unstable, or neutrally stable. In the last case, small effects connected with the finite shock wave thickness might affect the result. In studies of shock wave stability, it is natural to consider the gasdynamic discontinuity as the limiting case of a shock wave possessing internal structure. In particular, the stability of weak shock waves can be

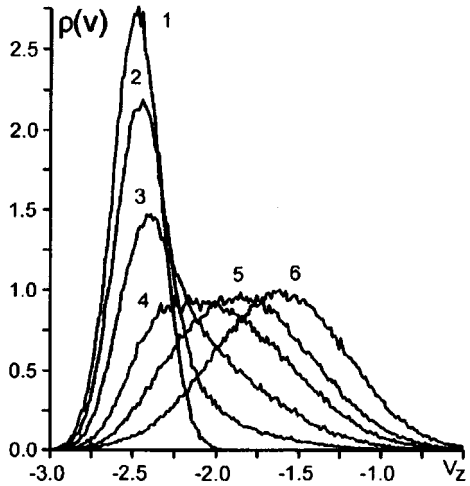

FIG. 3. Distribution functions of the z component of velocity in different layers normal to the z axis: *1*) $-12<z<-11.8$, *2*) $2<z<2.2$, *3*) $2.5<z<2.7$, *4*) $3<z<3.2$, *5*) $3.5<z<3.7$, *6*) $12<z<12.2$. Upstream velocity $|V_1|=2.48$.

studied using the Navier–Stokes equations. Effects of order l_s/λ, where λ is the perturbation wavelength, would be automatically taken into account in this study. This approach, however, cannot be directly applied to a shock wave of arbitrary amplitude in a medium with an arbitrary equation of state (which is of prime interest for shock instability studies). An alternative approach, which can be used in this case, is to study the stability problem for a gasdynamic discontinuity and incorporate the effect of finite shock thickness into the boundary conditions in the form of surface tension on a curved shock surface. The latter approach was used in Refs. 20 and 23 to account for the experimentally observed instability of the relaxation zone in ionizing shock waves in gases (note that in this case the relevant stability analysis can be performed in the hydrodynamic approximation). It is clear that the method based on the concept of surface tension offers considerable scope for the study of neutrally stable (according to Ref. 22) shock waves in liquids and solids. The values of γ calculated above can be used in such a study.

The evolution of the particle distribution over the velocity component v_z across the shock layer for $M\approx 2.5$ is shown in Fig. 3. It is easily seen that the distribution functions in different planes normal to the z axis are deviated widely from the corresponding bimodal distribution. A detailed comparison of the distribution functions derived from the MD simulation with those calculated using the bimodal distribution shows that, contrary to the case of gases,[16] the deviation decreases slightly with increasing Mach number.

Figure 4 shows the probability density for the potential energy in several planes $z=$ const within the shock layer. It is seen that the mean value of the potential energy is negative in the upstream flow and positive in the downstream flow, i.e., the shock compression of a liquid results in a change of sign of the interparticle forces. The corresponding change in the structure of the liquid is demonstrated in Fig. 5, where the evolution of the pair correlation function is shown. This is the correlation function that depends on

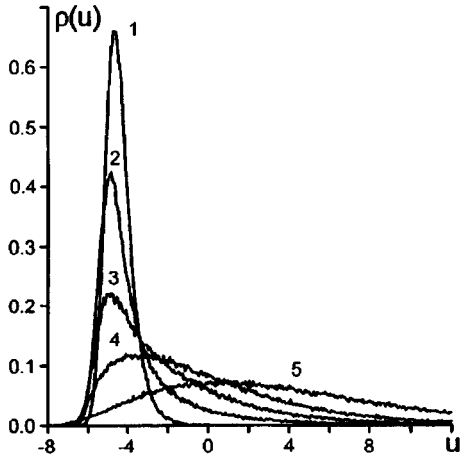

FIG. 4. Distribution functions of the potential energy in different layers normal to the z axis: *1*) $-12<z<1.18$, *2*) $2.5<z<2.7$, *3*) $3<z<3.2$, *4*) $3.5<z<3.7$, *5*) $12<z<12.2$. Upstream velocity $|V_1|=2.48$.

two-dimensional distance r between atoms in a plane $z=$ const. It is seen that the structure of the correlation functions is totally different from that observed in Ref. 16 for a shock wave in a dense gas. Curves *1* and *2* are closely similar to each other and are typical for the liquid state. Curve *3* shows that a short-range order exists in the shock-compressed fluid. Since the potential energy in the downstream flow is positive, the shock-compressed fluid resembles a system of closely packed spheres.

The authors would like to express their gratitude to A. F. Andreev, I. M. Khalatnikov, and L. P. Pitaevskiĭ for valuable discussions. The work was supported by the

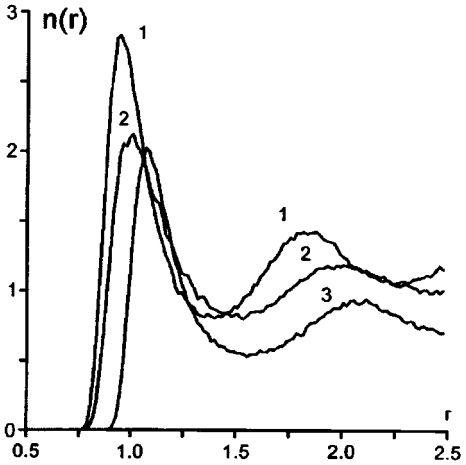

FIG. 5. The pair correlation function in the upstream *1*) $-12<z<-11.8$ and downstream *3*) $12<z<12.2$ flows, and at the center of shock layer *2*) $2<z<2.2$, $|V_1|=2.48$.

Cariplo Foundation for Scientific Research and the Russian Fund for Fundamental Research.

[a)]e-mail: anisimov@itp.ac.ru
[b)]e-mail: basil@landau.ac.ru

---

[1] E. Muntz and L. M. Harnett, Phys. Fluids **12,** 2027 (1969).
[2] L. D. Landau and E. M. Lifshitz, *Fluid Mechanics*, Pergamon Press, Oxford, 1959.
[3] H. W. Liepman, R. Narashima, and M. T. Chahine, Phys. Fluids **5,** 1313 (1962).
[4] D. Gilbarg and D. Paolucci, J. Ratl. Mech. Anal. **2**, 617 (1953).
[5] C. Muckenfuss, Phys. Fluids **5**, 1325 (1962).
[6] I. E. Tamm, Tr. Fiz. Inst. Akad. Nauk SSSR **29**, 317 (1965).
[7] H. M. Mott-Smith, Phys. Rev. **82**, 885 (1951).
[8] W. Fiszdon, R. Herczynski, and Z. Walenta, in *Rarefied Gas Dynamics*, Eds. M. Becker and M. Fiebig, Porz-Wahn, DFVLR Press, 1974, p. B23.
[9] G. A. Bird, Phys. Fluids **13**, 1172 (1979).
[10] W. G. Hoover, Phys. Rev. Lett. **42**, 1531 (1979).
[11] B. L. Holian, W. G. Hoover, B. Moran, and G. K. Straub, Phys. Rev. A **22**, 2798 (1980).
[12] E. Salomons and M. Marechal, Phys. Rev. Lett. **69**, 269 (1992).
[13] M. Koshi, T. Saito, H. Nagoya *et al.*, Kayakų Gakkaishi **55**, 229 (1994).
[14] V. V. Zhakhovskiĭ and S. I. Anisimov, Zh. Éksp. Teor. Fiz. **111**, 1328 (1997) [JETP **84**, 734 (1997)].
[15] D. W. Heerman, *Computer Simulation Methods in Theoretical Physics*, Springer Verlag, Berlin–New York, 1986.
[16] V. V. Zhakhovskii, K. Nishihara, and S. I. Anisimov, Phys. Rev. Lett., in press.
[17] S. I. Anisimov and V. V. Zhakhovskii, JETP Lett. **57**, 99 (1993).
[18] J. S. Rowlinson and B. Widom, *Molecular Theory of Capillarity*, Clarendon Press, Oxford, 1982.
[19] P. Resibois and M. De Lechner, *Classical Kinetic Theory of Fluids*, Wiley, New York, 1977.
[20] A. G. Bashkirov, *Nonequilibrium Statistical Mechanics of Heterogeneous Fluid Systems*, CRC Press, Boca Raton–London–Tokyo, 1995.
[21] W. M. Kornegay, J. D. Fridman, and W. C. Worthington, in *Proceedings of the 6th International Symposium on Rarefied Gas Dynamics*, 1969, Vol. 1, p. 863.
[22] S. P. Dyakov, Zh. Éksp. Teor. Fiz. **27**, 288 (1954).
[23] A. G. Bashkirov, Phys. Fluids A **3**, 960 (1991).

Published in English in the original Russian journal. Edited by Steve Torstveit.